# Bifurcation and deformation during the evolution of periodic patterns on a gel film bonded to a soft substrate

*Hiroaki Miyoshi*[1], *Seishiro Matsubara*[1], *Dai Okumura*[1, *]

[1] Department of Mechanical Systems Engineering, Nagoya University, Furo-cho, Chikusa-ku, Nagoya 464-8603, Japan

* Corresponding author.
E-mail address: dai.okumura@mae.nagoya-u.ac.jp (D. Okumura)

**Abstract**

In this study, we investigate the bifurcation and deformation during the evolution of periodic patterns on a gel film bonded to a soft substrate. 3D finite element analysis is performed using an inhomogeneous field theory for polymeric gels. Step-by-step eigenvalue buckling analysis is conducted to explore not only the first bifurcation, but also sequential bifurcations on bifurcated paths. When the hexagonal dimple mode occurs as the first bifurcation, the second bifurcation consists of rectangular checkerboard modes in three symmetric directions. The resulting deformation patterns are in good agreement with experiments and, surprisingly, are analogous to the in-plane buckling behavior of hexagonal honeycombs. Uniaxial, biaxial, and equibiaxial (flower-like) patterns are produced by the periodic arrangements of distorted dimples. The third and fourth bifurcations cause the coalescence of the selected dimples. This reveals the occurrence of the rectangular checkerboard modes at the second bifurcation to be the missing link in the pattern evolution from hexagonal dimples to herringbone and labyrinth patterns.

Keywords: Pattern evolution, Surface instability, Buckling, Bifurcation, Gels

## 1. Introduction

Highly ordered patterns with distinctive features emerge on the surface of stiff films bonded on soft substrates when buckling is caused by compressive stress in the film (Bowden et al., 1998; Huck et al., 2000; Yoo et al., 2002). Although classical buckling theory predicts simple wavelike patterns, such as stripe, checkerboard, and hexagonal patterns, associated with a critical stress (Allen, 1969), those observed are more complex such as herringbone, lamellar, and labyrinth patterns (Chen and Hutchinson, 2004; Audoly and Boudaund, 2008a). In experiments using gel films (Breid and Crosby, 2009,2011; Guvendiren et al., 2009,2010a,2010b), the emerging patterns were observed to evolve gradually as the compressive stress increased beyond the critical stress (i.e., as the overstress increased), because the stress was remotely controlled by the degree of swelling in the gel film. Specifically, hexagonal dimple patterns were observed to appear at small states of the overstress, whereas herringbone, lamellar, and labyrinth patterns appeared at large states of the overstress. Further, distinctive patterns, such as cage-, brick-, and peanut-like patterns, also appeared at intermediate states. According to Breid and Crosby (2009), the cage-like pattern consists of six coalesced pairs of dimples in a hexagon surrounding a single dimple. It is no doubtful that the mechanisms and hierarchical structures of the pattern evolutions should be investigated and understood by analytical and numerical approaches.

To understand the occurrence and evolution of the herringbone pattern, comparative analyses were performed by investigating the changes of the elastic energy and the buckling amplitude of the competing patterns, including herringbone, checkerboard, and hexagonal patterns, as a function of the overstress (Chen and Hutchinson, 2004; Cai et al., 2011). Chen and Hutchinson (2004) conducted postbuckling finite element analysis using a small initial imperfection prescribed by the surface deflection of each pattern, demonstrating that the herringbone pattern is dominant at high overstress. Cai et al., (2011) drew the same conclusion using an analytical upper-bound method. Further, they showed that at low overstress, the checkerboard pattern is dominant, whereas the hexagonal dimple pattern becomes dominant if the existence of an initial curvature of the film is assumed. This explains why the hexagonal dimple pattern is much more likely to be observed in experiments (Breid and Crosby, 2009,2011; Guvendiren et al.,

2009,2010a,2010b). These approaches are simple because they do not require the analysis of bifurcation points and modes. However, as mentioned by Chen and Hutchinson (2004), they do not elucidate how the herringbone pattern emerges at high overstress as the minimum energy pattern. The interactions of bifurcation modes caused by sequential bifurcations on bifurcated paths should be considered to elucidate the deformation process leading to the herringbone pattern.

Audoly and Boudaoud (2008a,2008b,2008c) carried out linear stability analysis of the straight-stripe buckling mode and pointed out that second bifurcations lead to the occurrence of undulating-stripe, varicose, checkerboard, and hexagonal buckling modes. They first showed that, although the straight-stripe mode is dominant at the first bifurcation under biaxial compressive stress in the film, the checkerboard mode becomes dominant under equibiaxial compression. This is because equibiaxial compression is in-plane and isotropic, and the checkerboard mode occurs through the superposition of two perpendicular sets of straight stripes (cf. hexagonal patterns, which are obtained by the superposition of three sets of straight stripes). By contrast, under biaxial but not equibaxial compression, the second bifurcation occurs with the undulating-stripe mode as the dominant buckling mode. Because the equibiaxial compressive stress of the film may not be perfectly isotropic owing to the presence of imperfections, the undulating-stripe mode can occur at the second bifurcation. Thus, the occurrence of the undulating-stripe mode is connected with the evolution of a herringbone pattern on the bifurcated path because the former mode can be regarded as a smooth and essential buckling mode leading to the evolution of the latter. These studies highlight the great importance of exploring not only the first bifurcation, but also sequential bifurcations occurring on bifurcated paths.

The detection of bifurcation points on a bifurcated path is still a challenge in 3D nonlinear finite element analysis because the bifurcation points are strongly affected by geometric and material nonlinearities, which are enhanced by pattern evolution (Xu et al., 2014,2015). In addition, pattern evolution is achieved by losing symmetry owing to multiple bifurcations. Thus, it is essential to analyze the multiplicity of bifurcations (Ohno et al., 2002; Okumura et al., 2004). To avoid bifurcation analysis, Chen and

Hutchinson (2004) and Cai et al., (2011) performed postbuckling analysis using the small initial imperfection prescribed by the predetermined pattern; in other studies, small random perturbations have been used as the small initial imperfection (Tallinen and Biggins, 2015; Budday et al., 2015, Zhao et al., 2019). By contrast, Xu et al., (2014,2015) analyzed sequential bifurcations on the bifurcated path of a film/substrate system using an approach based on the asymptotic numerical method (Damil and Potier-Ferry, 1990). Their approach introduces a fictitious perturbation force applied to a deformed state given as the base state to detect bifurcation points and modes on bifurcated paths. Okumura and Kasugai (2016) also proposed a similar but simpler approach using the finite element software Abaqus, which was referred to as step-by-step eigenvalue buckling analysis (Okumura et al., 2018). Introducing a dummy loading parameter into eigenvalue buckling analysis (using the BUCKLE option in Abaqus) enabled the analysis of bifurcation not only on bifurcated paths but also using the inhomogeneous field theory for polymeric gels, which is implemented into the user-defined subroutine UHYPER in Abaqus (Hong et al., 2009). Thus, the step-by-step eigenvalue buckling analysis using the inhomogeneous field theory for polymeric gels must elucidate the complex pattern evolutions observed in experiments (Breid and Crosby, 2009,2011; Guvendiren et al., 2009,2010a,2010b).

In this study, we investigate the bifurcation and deformation during the evolution of periodic patterns on a gel film bonded to a soft substrate. Section 2 briefly describes the inhomogeneous field theory for polymeric gels (Hong et al., 2009), which reproduces the swelling process of the gel film in 3D finite element analysis. In Section 3, we detail the procedures of eigenvalue buckling and postbuckling analyses (i.e., step-by-step eigenvalue buckling analysis; Okumura et al., (2016,2018)). Section 4 is devoted to numerical modeling. We focus on the hexagonal dimple mode at the first bifurcation because this pattern was observed in experiments (Breid and Crosby, 2009,2011; Guvendiren et al., 2009,2010a,2010b). This restriction prescribes the ratio of the in-plane lengths of periodic units. We consider the dominant wavelength (Allen, 1969; Chen and Hutchinson, 2004) by preparing a variety of periodic units with different lengths. Section 5 presents the results of the analysis obtained at the second bifurcation point and on the bifurcated paths. We find that the second bifurcation consists of

rectangular checkerboard modes in three symmetric directions, leading to a good understanding of the evolution of cage- and brick-like patterns (Breid and Crosby, 2009,2011). The resulting deformation patterns on the bifurcated paths are surprisingly analogous to the in-plane buckling behavior of hexagonal honeycombs (Gibson and Ashyby, 1997; Pakpa and Kyriakides, 1999; Ohno et al., 2002; Combescure et al., 2016,2020); that is, uniaxial, biaxial, and equibiaxial (flower-like) patterns are reproduced by the periodic arrangements of distorted dimples. Section 6 shows the results after the second bifurcation. The third and fourth bifurcations induce coalescence of the selected dimples. This reveals that the occurrence of the rectangular checkerboard modes at the second bifurcation is the missing link in the evolution from the hexagonal dimple pattern to the herringbone and labyrinth patterns. Finally, conclusions are presented in Section 7.

## 2. Inhomogeneous field theory

This section briefly describes the inhomogeneous field theory of polymeric gels in equilibrium (Hong et al., 2009). This theory considers that a polymer network is in contact with a solvent and subjected to mechanical loads and geometric constraints. When the stress-free, dry network is taken as a reference state, the deformation gradient of the network, $\mathbf{F}$, is defined as $F_{ij}=\mathrm{d}x_i(\mathbf{X})/\mathrm{d}X_j$, where $X_j$ and $x_i(\mathbf{X})$ are the network coordinates of a gel system in reference and deformed states, and $C(\mathbf{X})$ is defined as the concentration of solvent molecules at a point in the gel system. Because the two fields $x_i(\mathbf{X})$ and $C(\mathbf{X})$ characterize an equilibrium state, the free-energy density of the gel, $W$, is assumed to be a function of $\mathbf{F}$ and $C$, (i.e., $W(\mathbf{F}, C)$).

According to the Frenkel–Flory–Rehner hypothesis (Frenkel, 1940; Flory and Rehner, 1943), $W(\mathbf{F}, C)$ is assumed to consist of the sum of two terms associated with polymer stretching (i.e., the elastic strain energy, $W_\mathrm{e}(\mathbf{F})$) and the mixing of polymer and solvent molecules (i.e., the mixing energy, $W_\mathrm{m}(C)$). When the elastic and mixing contributions are physically derived from the Gaussian network theory (i.e., a Neo-Hookean solid model) and the Flory–Huggins solution theory, respectively (Flory and Rehner, 1943), the free energy function is written as

$$W = W_{\mathrm{e}} + W_{\mathrm{m}} = \frac{NkT}{2}(I - 3 - 2\log J) - \frac{kT}{\upsilon}\left[\upsilon C \log\left(1 + \frac{1}{\upsilon C}\right) + \frac{\chi}{1 + \upsilon C}\right], \tag{1}$$

where $I = F_{ij}F_{ij}$ and $J = \det \mathbf{F}$ are invariants of the deformation gradient, $N$ is the number of polymeric chains per reference volume, $kT$ is the absolute temperature in the unit of energy, $\upsilon$ is the volume per solvent molecule, and $\chi$ is the Flory–Huggins interaction parameter that characterizes the enthalpy of mixing. Eq. (1) shows the explicit form of $W$ as a function of $\mathbf{F}$ and $C$.

If $\delta x_i$ and $\delta C$ are considered to be arbitrary variations of $x_i$ and $C$ from an equilibrium state, the virtual work principle gives the following equilibrium equation in which the change of the free energy of the gel equals the sum of the work done by the external mechanical force and external solvent:

$$\int_V \delta W dV = \int_A t_i \delta x_i dA + \int_V q_i \delta x_i dV + \mu \int_V \delta C dV\,, \tag{2}$$

where $V$ is the reference volume and $A$ is the reference surface. The first and second terms on the right-hand side are the mechanical work done by surface traction $t_i$ and body forces $q_i$, respectively, and the third term represents the work done by the external solvent. Here, $\mu$ is the chemical potential of the external solvent, and is equivalent to that in the gel; that is,

$$\mu = \frac{\partial W}{\partial C}. \tag{3}$$

A Legendre transformation allows $W(\mathbf{F}, C)$ to be transformed into another form

$$\hat{W} = W - \mu C\,, \tag{4}$$

which is defined as a function of $\mathbf{F}$ and $\mu$ (i.e., $W(\mathbf{F}, \mu)$). The combination of Eqs. (2) and (4) leads to (Hong et al., 2009)

$$\int_V \delta \hat{W} dV = \int_A t_i \delta x_i dA + \int_V q_i \delta x_i dV\,. \tag{5}$$

When the gel is in an equilibrium state, the chemical potential of the solvent molecules in the gel is homogeneous and equals the chemical potential of the external solvent, $\mu$. Consequently, $\mu$ is regarded as a state variable, and the equilibrium condition in Eq. (5) takes the same form as that for a hyperelastic solid.

Assuming the incompressibility of a network of a polymer and liquid solvent, the volume of the gel is expressed as the sum of the volume of the dry network and that of the solvent (Treloar, 1975; Hong et al., 2009). The volume swelling ratio of the gel is equal to $J$ and is expressed as

$$J = 1 + \upsilon C . \tag{6}$$

Using Eqs. (1), (4) and (6), the free energy function can be rewritten as

$$\hat{W} = \frac{NkT}{2}(I - 3 - 2\log J) - \frac{kT}{\upsilon}\left[(J-1)\log\frac{J}{J-1} + \frac{\chi}{J}\right] - \frac{\mu}{\upsilon}(J-1), \tag{7}$$

which takes an explicit form as a function of $\mathbf{F}$ and $\mu$, and acts as a free-energy function for a compressible hyperelastic material because of the volumetric change induced by solvent absorption.

The swelling process is reproduced by increasing the value of $\mu$, because when $J$ =1, $\mu$ =–∞, and equilibrium swelling ($J$ >1) is approximately expressed as $\mu$ =0 (Hong, 2009; Kang and Huang, 2010a,2010b; Okumura et al., 2015). To avoid the singularity of $\mu$ =–∞ (Hong et al., 2009, Kang and Huang, 2010a), the free swelling state characterized by the homogeneous volume swelling ratio $J_0$ (>1) is used as a reference state (Hong et al., 2009). The homogenous deformation gradient is expressed as

$$F_{ij}^{0} = J_0^{1/3}\delta_{ij} , \tag{8}$$

where $\delta_{ij}$ is the Krönecker delta. In addition, the stress of the reference state is assumed to be homogeneously zero. Using Eqs. (1), (3), (6), and (8), a finite value of the chemical potential of the reference state, $\mu_0$, is obtained from

$$\frac{\mu_0}{kT} = N\upsilon\left(\frac{1}{J_0^{1/3}} - \frac{1}{J_0}\right) + \log\frac{J_0 - 1}{J_0} + \frac{1}{J_0} + \frac{\chi}{J_0^2}. \tag{9}$$

Eq. (8) allows the total deformation gradient to be expressible as $F_{ij} = F'_{ik} F^0_{kj}$, leading to $I = J_0^{2/3} I'$ and $J = J_0 J'$. Using the free swelling state with $J_0$ as the reference state, the free energy density of Eq. (7) is modified as $\hat{W}' = \hat{W} / J_0$; that is:

$$\hat{W}' = \frac{NkT}{2J_0}(J_0^{2/3} I' - 3 - 2\log(J_0 J')) - \frac{kT}{\upsilon}\left[(J' - J_0^{-1})\log\frac{J_0 J'}{J_0 J' - 1} + \frac{\chi}{J_0^2 J'}\right] - \frac{\mu}{\upsilon}(J' - J_0^{-1}), \tag{10}$$

Thus, the swelling process is reproduced by increasing the value of $\mu$ from $\mu_0$ to 0. Because we employ the finite element package Abaqus, Eq. (10) is implemented into the user-defined subroutine UHYPER and the value of $\mu$ is passed as an additional state variable. Although the two fields of the stress and volume swelling ratio are homogenous at the reference state (cf. Kang and Huang, 2010a), the two fields can become inhomogeneous via Abaqus analysis (Hong et al., 2009). It is noted that Eq. (1) is not always convex, especially depending on $\chi$. However, the incremental analysis in Abaqus using Eq. (4) (i.e., Eq. (10)) searches and finds the solution around the current configuration using relatively small increments so that the occurrence of unexpected solutions is excluded in Abaqus analysis.

## 3. Procedures of eigenvalue buckling and postbuckling analyses

This section describes the procedures of eigenvalue buckling and postbuckling analyses. Step-by-step eigenvalue buckling analysis is used to detect bifurcation points on bifurcated paths (Okumura et al., 2016,2018). As explained below, this analysis is conducted by introducing a dummy loading parameter into the eigenvalue buckling analysis (i.e., using the BUCKLE option in Abaqus, Appendix A). This introduction allows bifurcation analysis not only on bifurcated paths but also using the inhomogeneous field theory of polymeric gels (Section 2). Although this is conceptually

similar to the work of Xu et al., (2014, 2015), the procedure of Okumura et al., (2016,2018) can be implemented more simply.

First, we consider the eigenvalue buckling problem solved by the following finite element equations,

$$\{\mathbf{K}_0(\mathbf{P}) + \lambda_i \mathbf{K}_\Delta(\mathbf{P},\mathbf{Q})\}\boldsymbol{\phi}_i = \mathbf{0}, \tag{11}$$

which is available using the BUCKLE option in Abaqus (Appendix A). In Eq. (11), $\mathbf{K}_0(\mathbf{P})$ is the stiffness matrix at the base state, where $\mathbf{P}$ is the vector of nodal forces caused by preloads acting in the base state. By contract, $\mathbf{K}_\Delta(\mathbf{P},\mathbf{Q})$ is the differential stiffness matrix resulting from the incremental loading pattern $\mathbf{Q}$, which is the vector of nodal forces caused by incremental loads added at the base state (Appendix A). Thus, $\mathbf{K}_0(\mathbf{P})$ includes the effects of the geometric and material nonlinearities caused by the preloads, whereas $\mathbf{K}_\Delta(\mathbf{P},\mathbf{Q})$ is obtained by linear perturbation analysis when the incremental loads (i.e., $\mathbf{Q}$) are considered at the base state. Here, $\lambda_i$ and $\boldsymbol{\phi}_i$ are the eigenvalues (i.e., the multipliers of $\mathbf{Q}$) and the corresponding eigenvectors (i.e., the corresponding buckling modes), where $i$ indicates the $i$-th buckling mode and $\boldsymbol{\phi}_i$ are normalized such that the maximum displacement component is 1.

When the same loads are considered to the preloads and the incremental loads, Eq. (11) shows that the critical buckling loads are approximately estimated by extrapolation using $\mathbf{Q}$ from the base state described by $\mathbf{P}$. When $\det\{\mathbf{K}_0(\mathbf{P}) + \lambda_i \mathbf{K}_\Delta(\mathbf{P},\mathbf{Q})\} = 0$ is checked by changing the value of $\lambda_i$, the critical buckling loads are predicted as $\mathbf{P}+\lambda_i\mathbf{Q}$. If strong geometric and material nonlinearities appear during $\lambda_i\mathbf{Q}$, the predictions become less accurate as the value of $\lambda_i$ increases from 0 to a large value. By contrast, if the adjusted magnitude of $\mathbf{P}$ allows the resulting base state to be at a buckling point, the critical buckling load is just expressed by $\mathbf{P}$, removing the need of extrapolation of $\mathbf{Q}$. In this case, the effects of the geometric and material nonlinearities are included in the base state. Thus, accurate predictions are expected, although the magnitude of $\mathbf{P}$ must be adjusted by repeating step-by-step analysis. At least the minimum eigenvalue, $\lambda_1$, should be zero in Eq. (11). If multiple bifurcations are assumed as $\lambda_i = 0$ ($i$=1,2,3,…,$k$), Eq. (11) is simply reduced to

$$\mathbf{K}_0(\mathbf{P})\boldsymbol{\phi}_i = \mathbf{0} \quad \text{when } \lambda_i = 0 \qquad (i=1,2,3,\ldots,k). \tag{12}$$

Here, $k$ is the multiplicity of bifurcations. Eq. (12) results in $\det \mathbf{K}_0(\mathbf{P}) = 0$, which is the typical equation used to find the bifurcation points (Hill, 1958; Ohno et al., 2002; Okumura et al., 2004).

The inhomogeneous field theory for polymeric gels provides the chemical potential, $\mu$, as the loading parameter that reproduces the swelling process (Section 2); that is, the increase of $\mu$ is expected to be available to generate $\mathbf{P}$ and $\mathbf{Q}$. However, it is not available as $\mathbf{Q}$ because $\mathbf{K}_\Delta(\mathbf{P},\mathbf{Q})$ is obtained by linear perturbation analysis and the increase of $\mu$ is reflected only via the UHYPER (Appendix A; Abaqus 6.14; Okumura and Kasugai, 2016). For this reason, the variable of $\mu$ is only used to generate $\mathbf{P}$ as a function of $\mu_\mathrm{b}$ (i.e., $\mathbf{P}(\mu_\mathrm{b})$), where $\mu_\mathrm{b}$ is the value of $\mu$ at a base state. By contrast, an alternative variable (i.e., a dummy loading parameter) is needed to generate $\mathbf{Q}$ to mimic the volumetric increase caused by the increase of $\mu$.

To introduce a dummy loading parameter, we use the isotropic thermal expansion caused by the increase of temperature. The thermal expansion is modeled as $\alpha\Delta T$, where $\alpha$ is the thermal expansion coefficient and $\Delta T$ is the increase of temperature. The thermal expansion is considered to generate $\mathbf{Q}$ in the eigenvalue buckling analysis in Abaqus. When the value of $\alpha$ is used as the incremental load, $\mathbf{Q}$ is a function of $\mu_\mathrm{b}$ and $\alpha$ (i.e., $\mathbf{Q}(\mu_\mathrm{b},\alpha)$) because $\mathbf{Q}$ is solved by considering the incremental load $\alpha$ at the base state prescribed by $\mu_\mathrm{b}$ in linear perturbation analysis. The eigenvalues, $\lambda_i$, are directly associated with the increase of temperature, $\Delta T_i$, which is used as the dummy loading parameter. Thus, the critical buckling loads are expressed as $\mathbf{P}(\mu_\mathrm{b})+\Delta T_i\,\mathbf{Q}(\mu_\mathrm{b},\alpha)$. In this case, Eqs. (11) and (12) are rewritten as

$$\{\mathbf{K}_0(\mu_\mathrm{b}) + \Delta T_i\,\mathbf{K}_\Delta(\mu_\mathrm{b},\alpha)\}\boldsymbol{\phi}_i = \mathbf{0}, \tag{13}$$

$$\mathbf{K}_0(\mu_\mathrm{b})\boldsymbol{\phi}_i = \mathbf{0} \quad \text{when } \Delta T_i = 0 \qquad (i=1,2,3,\ldots,k). \tag{14}$$

Although the thermal expansion is similar to the expansion due to swelling, the former is homogeneous as a function of temperature, whereas the latter can become inhomogeneous as a function of the chemical potential (Hong et al., 2009). To detect accurate bifurcation points, the value of $\mu_b$ must be increased to decrease the lowest eigenvalue, $\Delta T_1$, to 0. Thus, eigenvalue buckling analysis (Eq. (13)) is performed using individual base states by the step-by-step increases of $\mu$. The base state with $\Delta T_1=0$ (in reality, it approximates zero) is regarded as the buckling point described by Eq. (14). We take the value of $\mu$ at this base state as the critical value of $\mu$. The deviations from the dummy loading parameter of $\Delta T_i$ as well as from extrapolation by $\mathbf{Q}(\mu_b,\alpha)$ from the base state are canceled by searching for the critical point expressed by Eq. (14). The multiplicity of bifurcations, $k$, is estimated by comparing $\Delta T_i$ ($i$=2,3,4,…) with $\Delta T_1$ at the critical base state. The multiple bifurcations may cause a loss of symmetry of the base state, such that the value of $k$ can also be determined by checking the buckling modes, $\boldsymbol{\phi}_i$ ($i$=1,2,3,…,$k$).

To perform postbuckling analysis on the evolution of the deformation pattern, the dominant buckling modes are introduced as a geometric imperfection (the IMPERFECTION option in Abaqus). When multiple bifurcations are considered (Eq. (14)), the imperfection, $\Delta\boldsymbol{\phi}$, introduced as initial geometrical imperfections, is expressed as

$$\Delta\boldsymbol{\phi} = dh\sum_{i=1}^{k} r_i\boldsymbol{\phi}_i\,, \tag{15}$$

where $h$ is the height of the initial gel film, $d$ is a small scaling factor, and $r_i$ are the coefficients that control the contributions of $\boldsymbol{\phi}_i$ ($i$=1,2,3,…,$k$). Further, because the present study focuses on the $n$-th bifurcation on the ($n$–1)-th bifurcated path, Eq. (15) is extended as

$$\Delta\boldsymbol{\phi}^{(n)} = dh\sum_{j=1}^{n}\sum_{i=1}^{k^{(j)}} r_i^{(j)}\boldsymbol{\phi}_i^{(j)}\,, \tag{16}$$

which we use as the initial geometric imperfections needed to trace the $n$-th bifurcated path. Here, $\boldsymbol{\phi}_i^{(j)}$ are the critical buckling modes at the $j$-th bifurcation point on the

($j$–1)-th bifurcated path (i.e., the 0-th bifurcated path is the primary path), where $k^{(j)}$ is the number of multiple bifurcations at the $j$–th bifurcation point, and $r_i^{(j)}$ are the coefficients that control the contributions of $\boldsymbol{\phi}_i^{(j)}$ ($i$=1,2,3,…,$k^{(j)}$). Our approach in this study enables the evolution of the deformation pattern to be investigated by repeating the eigenvalue buckling and postbuckling analyses on the bifurcated paths (Fig. 1). We note that $\boldsymbol{\phi}_i^{(j)}$ are the dominant buckling modes on the ($j$–1)-th bifurcated path and are not the higher-order buckling modes on the primary path.

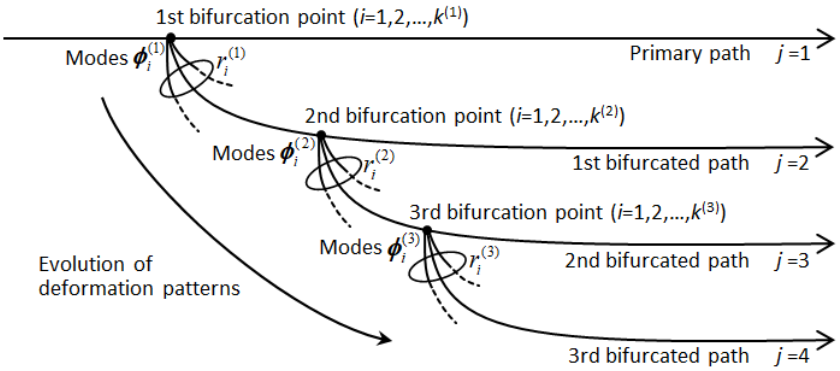


**Fig. 1.** Schematic illustration of the evolution of deformation patterns caused by multiple and sequential bifurcations. The dominant buckling modes are expressed as $\boldsymbol{\phi}_i^{(j)}$ ($i$=1,2,3,…,$k^{(j)}$), which occur at the $j$-th bifurcation point on the ($j$–1)-th bifurcated path. The multiplicity of bifurcations is expressed by $k^{(j)}$ such that there are many potential bifurcated paths, determined by the combination of $\boldsymbol{\phi}_i^{(j)}$ ($i$=1,2,3,…,$k^{(j)}$). The contributions are controlled by determining the coefficients, $r_i^{(j)}$ ($i$=1,2,3,…,$k^{(j)}$). As described in this section, the bifurcation points on the primary and bifurcated paths are detected by step-by-step eigenvalue buckling analysis, and pattern evolution is traced using the perturbation described by Eq. (16).

We use $d$= 0.005 or 0.01, which are smaller than the value of 0.02 used by Chen and Hutchinson (2004). To obtain a unique set of $r_i^{(j)}$, the ratios of $r_i^{(j)}$ ($i$=1,2,3,…,$k^{(j)}$) are first determined to generate a characteristic buckling mode, $\boldsymbol{\phi}_{\mathrm{X}}^{(j)}$, that consists of $\sum_{i=1}^{k^{(j)}} r_i^{(j)}\boldsymbol{\phi}_i^{(j)}$ ($i$=1,2,3,…,$k^{(j)}$), which is normalized such that the maximum displacement component of $\boldsymbol{\phi}_{\mathrm{X}}^{(j)}$ is 1.

Additionally, according to Healey (1989), the imperfection methods including the present approach (Eq. (16)) can fail to trace the bifurcated path related to the corresponding buckling mode. To avoid the possibility of accidental path switching, the pattern evolution in postbuckling should be compared with the imperfection generate by Eq. (16) (Sections 5 and 6).

## 4. Numerical modeling

### *4.1. Material properties*

To reproduce a gel film bonded on a soft substrate, the gel film is modeled using the inhomogeneous field theory for polymeric gels (Section 2), while the soft substrate is modeled using the incompressible Neo-Hookean solid model. The inhomogeneous field theory requires three material parameters, $N$, $\upsilon$ and $\chi$. The Young's modulus of the gel film, $E_f$, is related to $N$ as $E_f=3NkT$, where $kT=4\times10^{-21}$ J. We use a value of $N=0.125\times10^{27}$ m$^{-3}$ because $E_f=1.5$ MPa is regarded as a standard Young's modulus of PDMS materials (Okumura et al., 2015). The use of toluene as a specific organic solvent gives $\upsilon=1.76\times10^{-28}$ m$^3$, leading to a normalized Young's modulus of $E_f\,\upsilon/(3kT)=0.022$ (Okumura et al., 2015). In the present study, we focus on the pattern evolution caused by multiple and sequential bifurcations. Hence, we use a small value of $\chi=0.1$ to allow a large increase of the volume swelling ratio, $J$, when the swelling process is reproduced by increasing $\mu$ from $\mu_0$ to 0 (Section 2). Here, $J_0=1.003$ is used as an initial free swelling state such that Eq. (9) provides the initial value of $\mu$ as $\mu_0=-4.715kT$. For the soft substrate, the Young's modulus is assumed as $E_s=0.23$ MPa such that the ratio of the Young's moduli is $E_f/E_s=6.5$. Although our aim is not to undertake a qualitative discussion and comparison with experiments, a ratio of $E_f/E_s=6.5$ can be regarded as representative of films on soft substrates (Buddy et al., 2015).

### *4.2. Boundary and loading conditions*

Fig. 2 shows the periodic cells, used in 3D finite element analysis, which are rectangular parallelepiped and are defined by the individual lengths, $L_1$, $L_2$, $h$, and $H$. These lengths are normalized using $h$ (i.e., $L_1/h$, $L_2/h$ and $H/h$) (see Section 4.3). The gel film is perfectly bonded on the soft substrate ($x_3=H$). The bottom face of the soft substrate ($x_3=0$) has zero displacement, while the top face of the gel film ($x_3=h+H$) is stress free. Periodic boundary conditions are imposed on the side faces (the combination of $x_1=(0 \text{ or } L_1)$ or $x_2=(0 \text{ or } L_2)$), and are expressed as

$$\begin{cases} u_i(0,x_2,x_3)-u_i(L_1,x_2,x_3)=0 \\ u_i(x_1,0,x_3)-u_i(x_1,L_2,x_3)=0 \end{cases}, \tag{17}$$

where $u_i(x_1, x_2, x_3)$ is the displacement at a point $X_i$, defined as $u_i = x_i - X_i$. From the repulsive forces acting on the side faces, the in-plane components of the macroscopic nominal stress, $S_{11}^0$ and $S_{22}^0$, are calculated and used to estimate the critical value when bifurcation occurs (Section 4.3 and Appendix C).

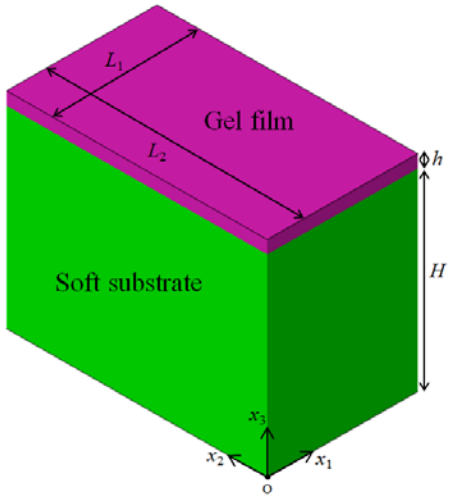


**Fig. 2.** Initial dimensions of the gel film bonded on the soft substrate. The individual lengths are normalized with respect to $h$ (i.e., $L_1/h$, $L_2/h$, and $H/h$). The value of $H/h$ is selected to be sufficiently large to avoid having to consider the effects of the constraint at the bottom face (Huang et al., 2005).

When the swelling process is simulated by incrementally increasing $\mu$ from $\mu_0$ to 0, the increase of $\mu$ causes an increase of the compressive stresses, $S_{11}^0$ and $S_{22}^0$; that is, buckling is caused by the in-plane compressive stresses produced in the gel film. The value of $\mu$ and change of $S_{11}^0 + S_{22}^0$ are used to estimate the bifurcation points and bifurcated paths. Automatic time incrementation is used in the Abaqus analysis. The value of $\mu$ is passed to UHYPER as an additional state variable. By contrast, step-by-step eigenvalue buckling analysis requires the temperature to increase to consider the isotropic thermal expansion as the dummy loading parameter (Section 3). The eigenvalues, $\Delta T_i$, are directly related to the increases of temperature, which are needed to generate the additional compressive stresses in the gel film and to extrapolate the bifurcation points. Because there is no reason to consider a specific value of the thermal expansion coefficient, $\alpha$, we arbitrarily set $\alpha$=0.01.

When postbuckling analysis is performed in Abaqus, the Riks method (i.e., the arc-length method) is usually used to have the ability to trace the bifurcated path with a discontinuous jump (i.e., with the decrease of the loading parameter). However, the chemical potential, $\mu$, is not a standard variable in Abaqus so that the present study cannot employ the Riks approach (Hong et al., 2009). Although the present study did not encounter this difficulty, if necessary, artificial damping can be used to solve this problem (Okumura et al., 2015).

*4.3. Dimensions of unit and periodic cells*

As mentioned in Section 1, we consider in the present study the occurrence of a hexagonal dimple mode at the first bifurcation point on the primary path (Breid and Crosby, 2009,2011; Guvendiren et al., 2009,2010a,2010b; Cai et al., 2011). Although the first bifurcation is known to consist of superposing sinusoidal wrinkle modes (i.e., straight stripe modes; Audoly and Boudaund, (2008a)) in all directions in the plane, the restriction of the hexagonal dimple mode allows the ratio of $L_2/L_1$ to be fixed as $L_2/L_1 = \sqrt{3}$ (Appendix B). The use of this ratio ensures that the hexagonal dimple mode consists of the superposition of individual sinusoidal wrinkle modes in the three symmetric directions. The wavelength, $\lambda$, is determined by the value of $L_2$ (i.e., $\lambda = 0.5L_2$) (Appendix B). According to Chen and Hutchinson (2004), the sinusoidal wrinkle modes have a dominant wavelength and the corresponding critical stress that can be analyzed by classical buckling analysis. When the thickness of the substrate is assumed to be infinite (i.e., $H/h \to \infty$), the dominant wavelength, $\lambda_{th}$, and the critical stress, $\sigma_{th}$, can be predicted as $\lambda_{th}/h = 2\pi(E_f/3E_s)^{1/3}$ and $\sigma_{th}/E_f = (1/3)(3E_s/E_f)^{2/3}$, respectively. Here, the Poisson's ratios for the film and substrate are assumed to be 0.5.

Although the value of $E_f/E_s = 6.5$ used in the present study gives $\lambda_{th}/h = 8.1$, the numerical predictions can deviate from this theoretical value because of the effects of the volumetric change due to swelling as well as the material nonlinearities of the film and substrate. To this end, Fig. 3a shows the unit cell and finite element meshes used to investigate the dominant wavelength of the hexagonal dimple mode. 3D finite element analysis is performed using the 8-node linear brick element with the element type C3D8RH. The numbers of nodes and elements are 31,226 and 28,800, respectively. The

same meshes are used for $L_2/h$=14,16,18,20,22, and 24. The value of $H/h$=15 is selected to be sufficiently large to avoid having to consider the effects of the constraint at the bottom face (Huang et al., 2005). The mesh resolution and the value of $H/h$=15 were determined by trial-and-error analysis to avoid high computational costs.

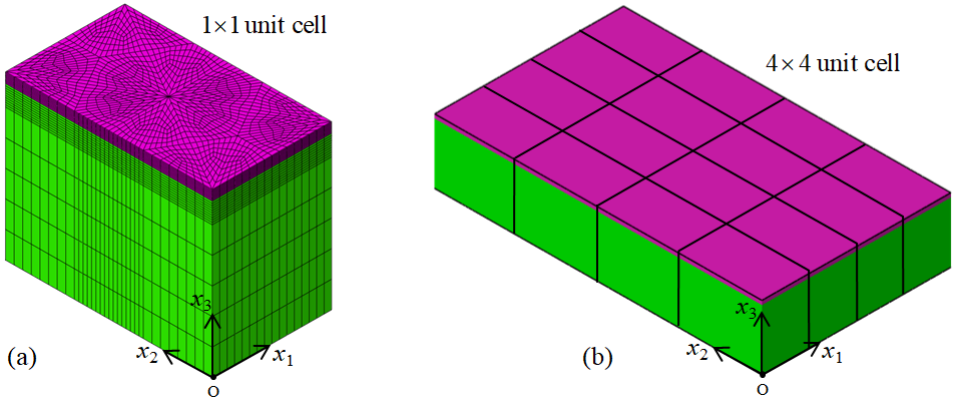


**Fig. 3.** Finite element meshes of the unit and periodic cells with $L_2/L_1=\sqrt{3}$ and $H/h$=15. (a) Unit cells with $L_2/h$=14,16,18,20,22, and 24. (b) Periodic cell consisting of 4×4 unit cells. Individual unit cells are analyzed to detect the dominant wavelength. The unit cell with $L_2/h$=20 produces the hexagonal dimple mode with a dominant wavelength of $\lambda_{cr}/h$=0.5 $L_2/h$ =10, which compares reasonably well the theoretical value (Appendix C). The length of the periodic cell is $L_2/h$=20×4=80.

As shown in Appendix C, the bifurcation points and modes at the first bifurcation on the primary path were analyzed by step-by-step eigenvalue buckling analysis. We found that the unit cell with $L_2/h$=20 produced the hexagonal dimple mode (Fig. C.3) with a dominant wavelength of $\lambda_{cr}/h$=0.5$L_2/h$ =10 (Fig. C.2). Bifurcation occurred at $\mu_{cr}/kT=\mu_b/kT$=–0.54 with $\left|S_{11}^0+S_{22}^0\right|_{cr}\upsilon/kT$ =0.0355, and $J_{cr}$=1.34 (Fig. C.1). The thickness of the gel film at the bifurcation point, $h^*$, was estimated as $h^*$=1.34$h$; the increase in thickness is attributed to swelling. When $h^*$ is introduced as $\lambda_{th}/h^*=2\pi(E_f/3E_s)^{1/3}$, the reduced nominal value (DuPont et al., 2010) yields $\lambda_{th}/h$=1.34 ×8.1=10.8. Because the material nonlinearities of the gel film and soft substrate are also expected to affect this bifurcation, we consider $\lambda_{cr}/h$=10 to be a reasonable value. Moreover, when $\sigma_{th}/E_f$ =(1/3)$(3E_s/E_f)^{2/3}$ is regarded as the value at the first bifurcation, the reduced nominal value is rewritten as $\sigma_{th}$ =1.34×(1/3) $E_f$ $(3E_s/E_f)^{2/3}$ =0.401 MPa. From $\left|S_{11}^0+S_{22}^0\right|_{cr}\upsilon/kT$ =0.0355, $\sigma_{cr}$=0.403 MPa is derived using $\sigma_{cr}=S_{11}^0=S_{22}^0$ at the first bifurcation, which is in good agreement with $\sigma_{th}$ =0.401 MPa.

To investigate the evolution of the periodic pattern from the hexagonal dimple mode, we analyze a large periodic cell consisting of 4×4 unit cells (Fig. 3b). Each unit cell has $L_2/h$ =20 with identical finite element meshes (i.e., Fig. 3a) such that the dimensions of the periodic cell are $L_2/h$ =80, $L_2/L_1=\sqrt{3}$, and $H/h$ =15. Because the unit cell is discretized using 31,226 nodes and 28,800 elements, the periodic cell, including 4×4 unit cells, is discretized using 484,250 nodes and 460,800 elements. In Sections 5 and 6, we refer to this periodic cell as a 4×4 unit cell to distinguish it from the 1×1 unit cell.

## 5. Results from the analysis of the second bifurcation

### *5.1. Second bifurcation on the first bifurcated path*

Fig. 4 shows the hexagonal dimple mode obtained from the 4×4 unit cell ($L_2/h$=80). The 4×4 unit cell shows the same bifurcation behavior as the 1×1 unit cell ($L_2/h$=20) (Appendix C). Regardless of the periodic arrangement of 4×4 unit cells, the dominant bifurcation mode is the hexagonal dimple mode expressed as $\boldsymbol{\phi}_{\text{hex}}^{(1)}=\boldsymbol{\phi}_{0}^{(1)}+\boldsymbol{\phi}_{60}^{(1)}+\boldsymbol{\phi}_{60^*}^{(1)}$. The first bifurcation for the 1×1 unit cell is understood as the superposition of the modes categorized by ($m$, $n$)=(0, 2) and ($m$, $n$)=(1, 1) with $\lambda/L_2$=0.5 and $M$=6 (Appendix B). Similarly, the bifurcation for the 4×4 unit cell is understood as the superposition of ($m$, $n$)=(0, 8) and ($m$, $n$)=(4, 4) with $\lambda/L_2$=0.125 and $M$=6. In both cases, the wavelength and the three wave directions are $\lambda/h$=10 and $\psi$=0°, ±60°, respectively. Here, $M$ is the multiplicity of bifurcations. This result shows that the sinusoidal wrinkle modes with $\lambda/h$=10 appear preferentially at the first bifurcation point (Chen and Hutchinson, 2004). In addition, eigenvalue analysis predicts that the first bifurcation point has a sextuple bifurcation as $k^{(1)}$=6, which is consistent with $M$=6. The unique hexagonal dimple mode (Fig. 4) is obtained by controlling the individual phase shifts to assign the dimple at the center of each unit cell included in the 4×4 unit cell (Appendix C).

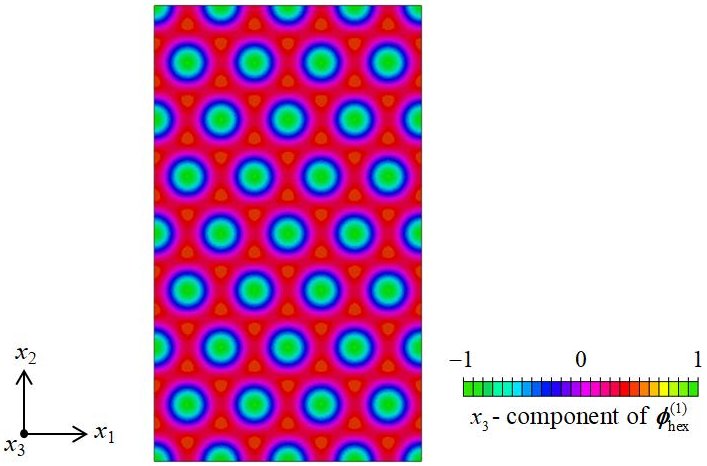


**Fig. 4.** Hexagonal dimple mode, $\phi^{(1)}_{hex}$, analyzed for the first bifurcation at $\mu_b/kT$=–0.54 on the primary path. The 4×4 unit cell with $L_2/h$=80 results in $\lambda/L_2$=0.125 ($M$=6). The dominant wavelength is $\lambda/h$=10(=0.125×80) because this mode is identical to that obtained by $\lambda/L_2$=0.5 ($M$=6) with $L_2/h$=20. The hexagonal dimple mode consists of a superposition of sinusoidal wrinkle modes in three symmetric directions, 0° and ± 60° (i.e., $\phi^{(1)}_{hex} = \phi^{(1)}_{0} + \phi^{(1)}_{60} + \phi^{(1)}_{60^*}$) (Appendices B and C).

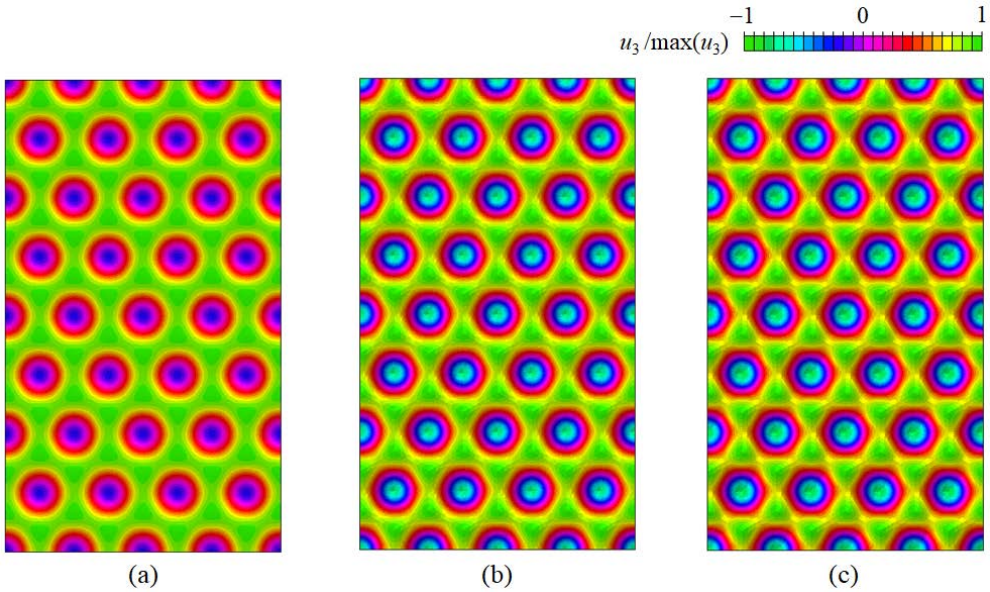


**Fig. 5.** Evolution of the deformation pattern on the first bifurcated path. (a) $\mu/kT$=–0.54, (b) $\mu/kT$=–0.39 (the second bifurcation point), and (c) $\mu/kT$=–0.29. Postbuckling analysis is performed using the hexagonal dimple mode, $\phi^{(1)}_{hex}$, as the initial imperfections. The second bifurcation is detected using step-by-step eigenvalue buckling analysis. The base state of $\mu/kT$=–0.39 is the second bifurcation point on the first bifurcated path.

Fig. 5 shows the evolution of the deformation pattern from the primary path to the first bifurcated path. The second bifurcation point is successfully detected at this base state (Fig. 5b). Fig. 6 shows the bifurcation modes obtained at the second bifurcation

point. Because this bifurcation point is estimated to be a triple bifurcation (i.e., $k^{(2)}$=3), Fig. 6a–c shows three independent modes, $\boldsymbol{\phi}_{\mathrm{cb0}}^{(2)}$, $\boldsymbol{\phi}_{\mathrm{cb60}}^{(2)}$, and $\boldsymbol{\phi}_{\mathrm{cb60*}}^{(2)}$, respectively. The individual modes are found to have the same checkerboard mode oriented in specific directions. The arrows in Fig. 6a–c depict the representative direction of each checkerboard mode. The characteristic directions of $\boldsymbol{\phi}_{\mathrm{cb0}}^{(2)}$, $\boldsymbol{\phi}_{\mathrm{cb60}}^{(2)}$, and $\boldsymbol{\phi}_{\mathrm{cb60*}}^{(2)}$ have angles of 0° and $\pm$60°, respectively. We attribute this to the deformation pattern caused by the hexagonal dimple mode maintaining hexagonal symmetry (Ohno et al., 2002; Okumura et al., 2002).

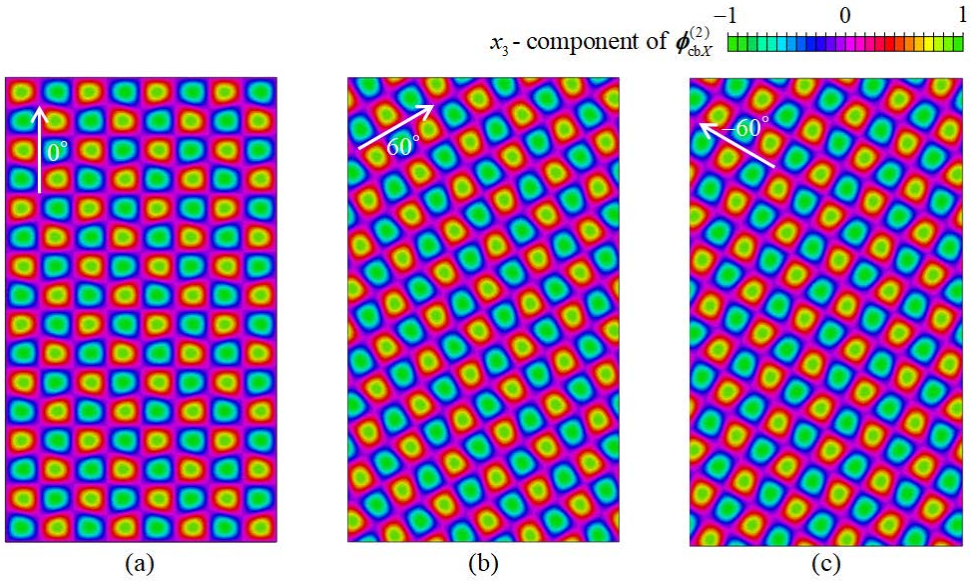


**Fig. 6.** Three rectangular checkerboard modes analyzed for the second bifurcation at $\mu_{\mathrm{b}}/kT$=−0.39 on the first bifurcated path. (a) $\boldsymbol{\phi}_{\mathrm{cb0}}^{(2)}$, (b) $\boldsymbol{\phi}_{\mathrm{cb60}}^{(2)}$, and (c) $\boldsymbol{\phi}_{\mathrm{cb60*}}^{(2)}$. The arrows oriented with the angles of 0°, $\pm$60° depict the respective directions of the individual modes. The second bifurcation point is estimated as $k^{(2)}$=3 (i.e., a triplet bifurcation), and is interpreted as the selected combination of the modes categorized by ($m$, $n$)=(2, 10), ($m$, $n$)=(4, 8), and ($m$, $n$)=(6, 2) ($M$=4+4+4=12) with $L_2/h$=80 (Appendix D). The individual wrinkle modes have the same wavelength as $\lambda/h$=7.6 (cf. $\lambda/h$=10 for the hexagonal dimple mode). $M$=12 is reduced to $k^{(2)}$=3 because of the presence of the hexagonal dimples. Three rectangular checkerboard modes, $\boldsymbol{\phi}_{\mathrm{cb0}}^{(2)}$, $\boldsymbol{\phi}_{\mathrm{cb60}}^{(2)}$, and $\boldsymbol{\phi}_{\mathrm{cb60*}}^{(2)}$, are allowed to occur selectively.

When the resulting checkerboard modes (Fig. 6) are compared with the sinusoidal wrinkle modes categorized by $m$ and $n$ (Appendix B), the second bifurcation point is found to be interpreted as the selected combination of the modes categorized by ($m$, $n$)=(2, 10), ($m$, $n$)=(4, 8), and ($m$, $n$)=(6, 2) (Appendix D) (i.e., $M$=4+4+4=12). The individual wrinkle modes have the same wavelength (i.e., $\lambda/h$=7.6). The wave directions

for ($m$, $n$)=(2, 10), (4, 8) and (6, 2) are prescribed by the angles $\pm 19°$, $\pm 41°$, and $\pm 79°(=\mp 101°)$, respectively. As described in Appendix D, $\boldsymbol{\phi}^{(2)}_{\mathrm{cb0}}$ consists of the two wrinkle modes prescribed by $\pm 41°$, whereas $\boldsymbol{\phi}^{(2)}_{\mathrm{cb60}}$ and $\boldsymbol{\phi}^{(2)}_{\mathrm{cb60*}}$ consist of those prescribed by 19° and −79°(=101°), and −19° and 79°(=−101°), respectively. Because the two wave directions are not orthogonal, $\boldsymbol{\phi}^{(2)}_{\mathrm{cb0}}$, $\boldsymbol{\phi}^{(2)}_{\mathrm{cb60}}$, and $\boldsymbol{\phi}^{(2)}_{\mathrm{cb60*}}$ produce a rectangular checkerboard mode. The representative directions of $\boldsymbol{\phi}^{(2)}_{\mathrm{cb0}}$, $\boldsymbol{\phi}^{(2)}_{\mathrm{cb60}}$, and $\boldsymbol{\phi}^{(2)}_{\mathrm{cb60*}}$ (Fig. 6a–c) are confirmed as $0°=(41°-41°)/2$ and $\pm 60°=\pm(19°+101°)/2$, respectively. At the second bifurcation point, the same rectangular checkerboard mode occurs in the three symmetric directions, resulting in either the retention or loss of hexagonal symmetry.

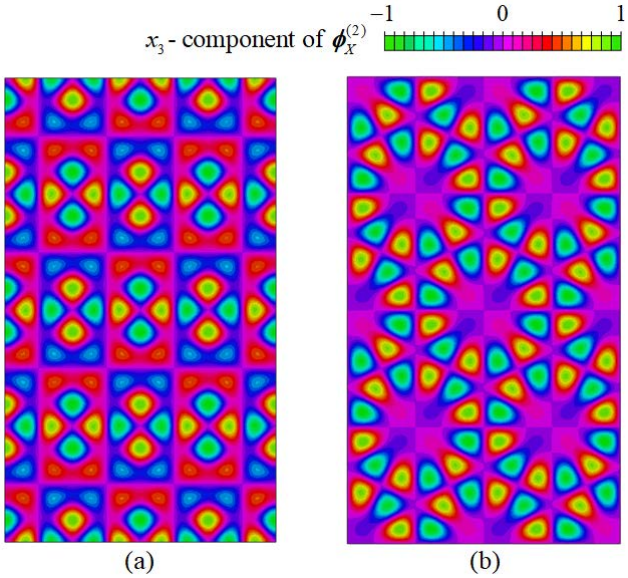


**Fig. 7.** Modes II and III obtained by superposing the rectangular checkerboard modes, $\boldsymbol{\phi}^{(2)}_{\mathrm{cb0}}$, $\boldsymbol{\phi}^{(2)}_{\mathrm{cb60}}$ and $\boldsymbol{\phi}^{(2)}_{\mathrm{cb60*}}$. (a) Mode II ($\boldsymbol{\phi}^{(2)}_{\mathrm{II}} = -\boldsymbol{\phi}^{(2)}_{\mathrm{cb60}} + \boldsymbol{\phi}^{(2)}_{\mathrm{cb60*}}$) and (b) Mode III ($\boldsymbol{\phi}^{(2)}_{\mathrm{III}} = \boldsymbol{\phi}^{(2)}_{\mathrm{cb0}} + \boldsymbol{\phi}^{(2)}_{\mathrm{cb60}} + \boldsymbol{\phi}^{(2)}_{\mathrm{cb60*}}$). Mode I is expressed as $\boldsymbol{\phi}^{(2)}_{\mathrm{I}} = \boldsymbol{\phi}^{(2)}_{\mathrm{cb0}}$ (Fig. 6a). Modes II and III become complex and yield beautiful patterns. It is extremely unlikely that pattern evolution is caused by the occurrence of $\boldsymbol{\phi}^{(2)}_{\mathrm{I}}$, $\boldsymbol{\phi}^{(2)}_{\mathrm{II}}$ and $\boldsymbol{\phi}^{(2)}_{\mathrm{III}}$ at the second bifurcation subsequent to the occurrence of the hexagonal dimple mode, $\boldsymbol{\phi}^{(1)}_{\mathrm{hex}}$, at the first bifurcation. Postbuckling analysis is performed using the initial imperfections prescribed by $\boldsymbol{\phi}^{(2)}_{\mathrm{I}}$, $\boldsymbol{\phi}^{(2)}_{\mathrm{II}}$, and $\boldsymbol{\phi}^{(2)}_{\mathrm{III}}$, as well as $\boldsymbol{\phi}^{(1)}_{\mathrm{hex}}$.

### *5.2. Pattern evolution on the second bifurcated paths (Modes I, II, and III)*

At the second bifurcation point, the bifurcation modes are arbitrarily generated by the superposition of the three rectangular checkerboard modes, $\boldsymbol{\phi}^{(2)}_{\mathrm{cb0}}$, $\boldsymbol{\phi}^{(2)}_{\mathrm{cb60}}$, and $\boldsymbol{\phi}^{(2)}_{\mathrm{cb60*}}$. We focus on typical cases, referred to as Modes I, II, and III, which are expressed as $\boldsymbol{\phi}^{(2)}_{\mathrm{I}} = \boldsymbol{\phi}^{(2)}_{\mathrm{cb0}}$, $\boldsymbol{\phi}^{(2)}_{\mathrm{II}} = -\boldsymbol{\phi}^{(2)}_{\mathrm{cb60}} + \boldsymbol{\phi}^{(2)}_{\mathrm{cb60*}}$ (this is periodically the same as $\boldsymbol{\phi}^{(2)}_{\mathrm{cb60}} + \boldsymbol{\phi}^{(2)}_{\mathrm{cb60*}}$), and

$\boldsymbol{\phi}_{\mathrm{III}}^{(2)} = \boldsymbol{\phi}_{\mathrm{cb0}}^{(2)} + \boldsymbol{\phi}_{\mathrm{cb60}}^{(2)} + \boldsymbol{\phi}_{\mathrm{cb60*}}^{(2)}$ (Fig. 6a and Fig. 7). The resulting modes become complex and yield beautiful patterns. It is highly unlikely that pattern evolution is caused by the occurrence of $\boldsymbol{\phi}_{\mathrm{I}}^{(2)}$, $\boldsymbol{\phi}_{\mathrm{II}}^{(2)}$ and $\boldsymbol{\phi}_{\mathrm{III}}^{(2)}$ at the second bifurcation subsequent to the occurrence of the hexagonal dimple mode, $\boldsymbol{\phi}_{\mathrm{hex}}^{(1)}$, at the first bifurcation. Thus, we perform postbuckling analysis using the initial imperfections prescribed by $\boldsymbol{\phi}_{\mathrm{I}}^{(2)}$, $\boldsymbol{\phi}_{\mathrm{II}}^{(2)}$, and $\boldsymbol{\phi}_{\mathrm{III}}^{(2)}$, as well as $\boldsymbol{\phi}_{\mathrm{hex}}^{(1)}$.

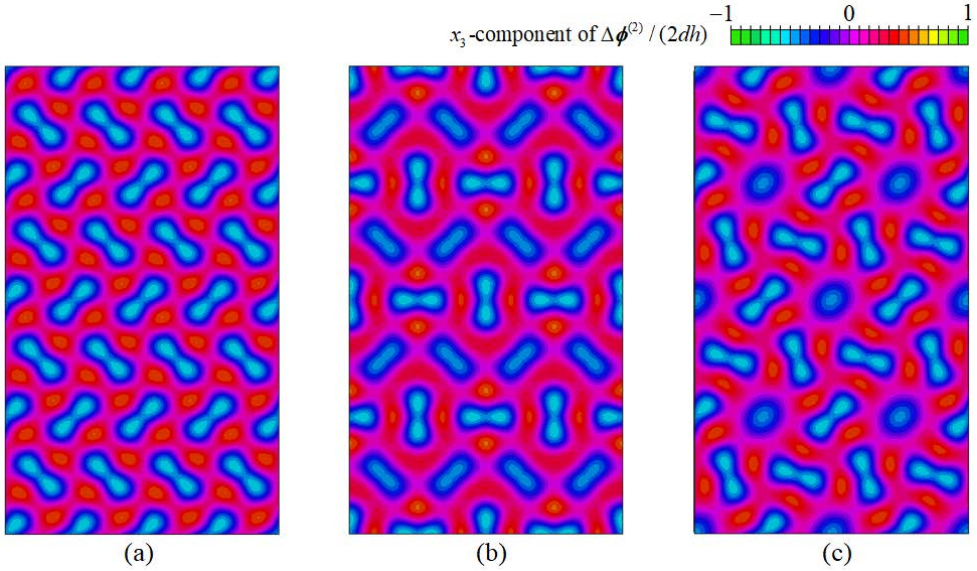


**Fig. 8.** Imperfections introduced to perform postbuckling analysis of Modes I, II, and III. (a) $\boldsymbol{\phi}_{\mathrm{hex}}^{(1)} + \boldsymbol{\phi}_{\mathrm{I}}^{(2)}$, (b) $\boldsymbol{\phi}_{\mathrm{hex}}^{(1)} + \boldsymbol{\phi}_{\mathrm{II}}^{(2)}$, and (c) $\boldsymbol{\phi}_{\mathrm{hex}}^{(1)} + \boldsymbol{\phi}_{\mathrm{III}}^{(2)}$. Although $\boldsymbol{\phi}_{\mathrm{hex}}^{(1)}$ only expresses the periodic arrangement of the circular dimples, the combination of $\boldsymbol{\phi}_{\mathrm{hex}}^{(1)} + \boldsymbol{\phi}_{\mathrm{I}}^{(2)}$, $\boldsymbol{\phi}_{\mathrm{hex}}^{(1)} + \boldsymbol{\phi}_{\mathrm{II}}^{(2)}$, and $\boldsymbol{\phi}_{\mathrm{hex}}^{(1)} + \boldsymbol{\phi}_{\mathrm{III}}^{(2)}$ distorts the circular dimples in specific directions. Surprisingly, these imperfections are similar to the buckling modes that occur in hexagonal honeycombs subjected to in-plane compression (Gibson ant Asyby, 1997; Papka and Kyriakides, 1999; Ohno et al., 2002; Okumrua et al., 2002; Combescure et al., 2016,2020). We refer to $\boldsymbol{\phi}_{\mathrm{hex}}^{(1)} + \boldsymbol{\phi}_{\mathrm{III}}^{(2)}$ as the flower-like mode, whereby the center dimple is surrounded by six distorted dimples, giving the appearance of a flower.

Fig. 8 shows the initial imperfections introduced to perform the postbuckling analysis of Modes I, II, and III (i.e., $\boldsymbol{\phi}_{\mathrm{hex}}^{(1)} + \boldsymbol{\phi}_{\mathrm{I}}^{(2)}$, $\boldsymbol{\phi}_{\mathrm{hex}}^{(1)} + \boldsymbol{\phi}_{\mathrm{II}}^{(2)}$, and $\boldsymbol{\phi}_{\mathrm{hex}}^{(1)} + \boldsymbol{\phi}_{\mathrm{III}}^{(2)}$, respectively). Comparison of Fig 8 with Fig. 4 reveals that $\boldsymbol{\phi}_{\mathrm{hex}}^{(1)}$ only expresses the hexagonal arrangement of the circular dimples, whereas $\boldsymbol{\phi}_{\mathrm{hex}}^{(1)} + \boldsymbol{\phi}_{\mathrm{I}}^{(2)}$, $\boldsymbol{\phi}_{\mathrm{hex}}^{(1)} + \boldsymbol{\phi}_{\mathrm{II}}^{(2)}$, and $\boldsymbol{\phi}_{\mathrm{hex}}^{(1)} + \boldsymbol{\phi}_{\mathrm{III}}^{(2)}$ distort the circular dimples in specific directions. Surprisingly, although the hexagonal dimples are not hexagonal honeycombs, the initial imperfections (Fig. 8) are highly similar to the buckling modes that occur in hexagonal honeycombs subjected to in-plane compression (Gibson ant Asyby, 1997; Papka and Kyriakides, 1999; Ohno et al., 2002;

Okumrua et al., 2002; Combescure et al., 2016,2020). In the case of honeycomb buckling, Modes I, II, and III are called uniaxial, biaxial and equibiaxial buckling modes. Mode III is also called the flower-like mode (Papka and Kyriakides, 1999), whereby the center cell or dimple, which is rarely distorted, is surrounded by six distorted cells or dimples, giving the appearance of a flower (Fig. 8c). In addition, the uniaxial mode allows the distorted dimples to be alternately oriented in the vertical direction (Fig. 8a). This means that although the hexagonal honeycombs have Modes I, II, and III as the dominant modes at the first bifurcation point, the flat gel film has Modes I, II, and III as the imperfections introduced from the combination of the dominant modes at the first and second bifurcation points. The hexagonal dimple mode, $\boldsymbol{\phi}_{\mathrm{hex}}^{(1)}$, is needed to form a hexagonal dimple structure on the flat gel film at the first bifurcation point, whereas the rectangular checkerboard modes, $\boldsymbol{\phi}_{\mathrm{cb0}}^{(2)}$, $\boldsymbol{\phi}_{\mathrm{cb60}}^{(2)}$, and $\boldsymbol{\phi}_{\mathrm{cb60*}}^{(2)}$, are needed to distort the circular dimples, which lead to the pattern evolution of the uniaxial, biaxial and equibiaxial (flower-like) modes on the second bifurcated path, as described below.

Fig. 9 shows the pattern evolution on the second bifurcated paths analyzed for Modes I, II, and III. The uniaxial, biaxial and equibiaxial (flower-like) patterns observed for the hexagonal honeycombs appear on the surface of the gel film. These deformation patterns are generated by $\boldsymbol{\phi}_{\mathrm{hex}}^{(1)}$ as the first bifurcation and $\boldsymbol{\phi}_{\mathrm{cb0}}^{(2)}$, $\boldsymbol{\phi}_{\mathrm{cb60}}^{(2)}$, and $\boldsymbol{\phi}_{\mathrm{cb60*}}^{(2)}$ as the second bifurcation. Notably, $\boldsymbol{\phi}_{\mathrm{hex}}^{(1)}$ consists of the sinusoidal wrinkle modes in the three symmetric directions with $\lambda/h$=10 (Appendices B and C), and $\boldsymbol{\phi}_{\mathrm{cb0}}^{(2)}$, $\boldsymbol{\phi}_{\mathrm{cb60}}^{(2)}$, and $\boldsymbol{\phi}_{\mathrm{cb60*}}^{(2)}$ consist of the rectangular checkerboard modes in the same three directions, which also consist of the superposition of the two sinusoidal wrinkle modes with $\lambda/h$=7.6 (Appendix D). We emphasize that the deformation patterns (Fig. 9) are in very good agreement with experiments reported by Breid and Crosby (2009,2011). The observed cage- and brick-like patterns appear when the circular dimples are distorted by the occurrence of the second bifurcation. These patterns are similar to the flower-like pattern (Mode III) and the uniaxial and biaxial patterns (Modes I and II), respectively.

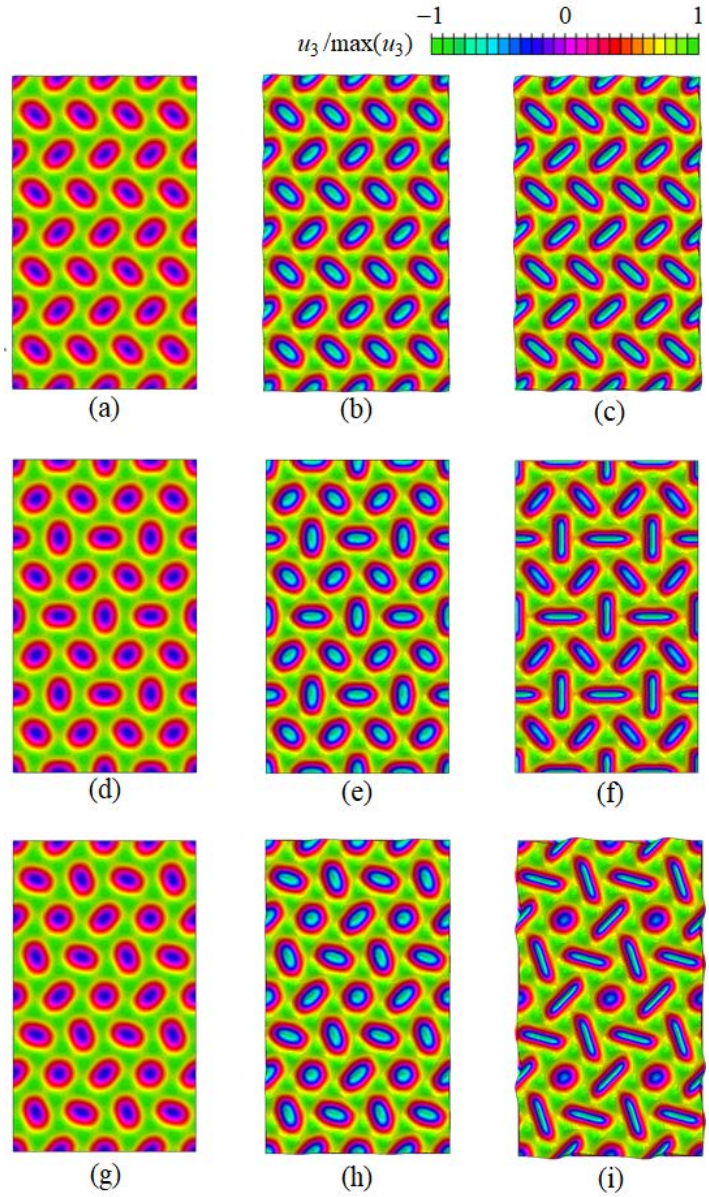


**Fig. 9.** Pattern evolution on the second bifurcated paths for Mode I ((a) $\mu/kT$=–0.54, (b) $\mu/kT$=–0.37, and (c) $\mu/kT$=–0.31); Mode II ((d) $\mu/kT$=–0.54, (e) $\mu/kT$=–0.38, and (f) $\mu/kT$=–0.28); and Mode III ((g) $\mu/kT$=–0.54, (h) $\mu/kT$=–0.39, and (i) $\mu/kT$=–0.28). Incredibly, the uniaxial, biaxial and equibiaxial (flower-like) patterns observed for the hexagonal honeycombs appear on the surface of the gel film. These deformation patterns are generated by $\boldsymbol{\phi}_{\mathrm{hex}}^{(1)}$ at the first bifurcation and $\boldsymbol{\phi}_{\mathrm{cb0}}^{(2)}$, $\boldsymbol{\phi}_{\mathrm{cb60}}^{(2)}$, and $\boldsymbol{\phi}_{\mathrm{cb60*}}^{(2)}$ at the second bifurcation. The deformation patterns are in very good agreement with experiments by Breid and Crosby (2009,2011). Cage- and brick-like patterns appear when the circular dimples are distorted by the occurrence of the second bifurcation.

Fig. 10 shows the change of the in-plane compressive stress, $\left|S_{11}^0+S_{22}^0\right|\upsilon/kT$, as a function of the chemical potential, $\mu/kT$. The primary and first bifurcated paths are also depicted with the first and second bifurcation points. The deformation patterns on the

first and second bifurcated paths are also depicted in the figure. The differences between the second bifurcated paths for Modes I, II, and III are almost negligible. Thus, it does not make sense to discuss the dominant pattern among Modes I, II, and III. As mentioned above, a similar variety of deformation patterns, including cage- and brick-like patterns, has been observed in experiments (Breid and Crosby, 2009,2011). Thus, in the next section (Section 6), we analyze the pattern evolution caused by further bifurcations on the second bifurcated paths generated by Modes I, II, and III.

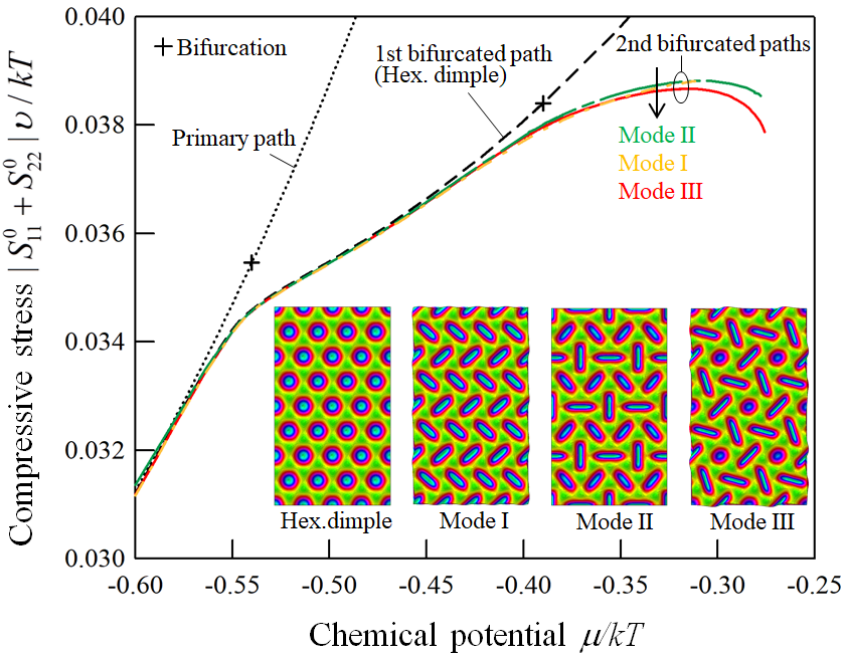


**Fig. 10.** Change of the in-plane compressive stress, $\left|S_{11}^0 + S_{22}^0\right|\upsilon / kT$, as a function of the chemical potential, $\mu/kT$. The primary and first bifurcated paths are also depicted with the first and second bifurcation points. The second bifurcated paths for Modes I, II, and III are hardly distinguishable. A similar variety of deformation patterns, including cage- and brick-like patterns, has been observed in experiments (Breid and Crosby, 2009,2011).

## 6. Pattern evolution caused by further bifurcations

### *6.1. Pattern evolution from Mode I*

The third bifurcation point on the second bifurcated path generated by Mode I (Fig. 9a–c) is obtained as $k_{\mathrm{I}}^{(3)}=1$ (i.e., a single bifurcation). Fig. 11a shows the third bifurcation mode, $\boldsymbol{\phi}_{\mathrm{I}}^{(3)}$, and Fig. 11b shows the imperfections prescribed by $\boldsymbol{\phi}_{\mathrm{hex}}^{(1)}+\boldsymbol{\phi}_{\mathrm{I}}^{(2)}+\boldsymbol{\phi}_{\mathrm{I}}^{(3)}$, which are used to trace the third bifurcated path. The bifurcation mode can be viewed as a varicose stripe mode (Audoly and Boudaund, 2008a). Further, the

mode may be compared with the sinusoidal wrinkle modes categorized by $m$ and $n$ (Appendices B and D). However, because this mode occurs as a single bifurcation, Fig. 11 simply shows that when $\boldsymbol{\phi}_{\mathrm{I}}^{(3)}$ interacts with the deformation pattern for Mode I (Fig. 9a–c) on the third bifurcated path, this varicose stripe mode enables the distorted dimples to coalesce along the vertical direction. The resulting zigzag grooves are periodically arranged in the horizontal direction. In other words, the occurrence of a herringbone pattern is expected on the third bifurcated path and is confirmed by postbuckling analysis.

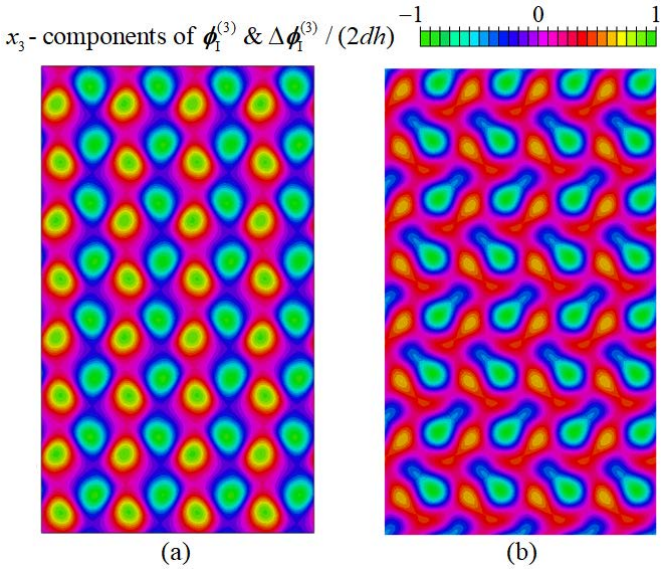


**Fig. 11.** The bifurcation mode at the third bifurcation point analyzed from Mode I and the imperfections used to analyze the third bifurcated path. (a) $\boldsymbol{\phi}_{\mathrm{I}}^{(3)}$ and (b) $\boldsymbol{\phi}_{\mathrm{hex}}^{(1)}+\boldsymbol{\phi}_{\mathrm{I}}^{(2)}+\boldsymbol{\phi}_{\mathrm{I}}^{(3)}$. The varicose stripe mode enables the distorted dimples (Fig. 9a–c) to coalesce along the vertical direction. In other words, the occurrence of a herringbone pattern is expected to occur on the third bifurcated path and is confirmed by postbuckling analysis (Fig. 12).

Fig. 12 shows the pattern evolution obtained by postbuckling analysis using the imperfections of $\boldsymbol{\phi}_{\mathrm{hex}}^{(1)}+\boldsymbol{\phi}_{\mathrm{I}}^{(2)}+\boldsymbol{\phi}_{\mathrm{I}}^{(3)}$. Fig. 12 confirms that the distorted dimples coalesce along the vertical direction to generate a herringbone pattern. The mechanism by which the herringbone pattern formed is described as follows. First, the hexagonal dimple pattern appears at the first bifurcation point. Second, the individual circular dimples are distorted at the second bifurcation point. The resulting pattern is similar with the uniaxial buckling mode that occurs in hexagonal honeycombs (Gibson and Ashby, 1997). The distorted dimples then coalesce along the vertical direction on the

third bifurcated path. This coalescence yields periodically arranged zigzag grooves (i.e., the herringbone pattern).

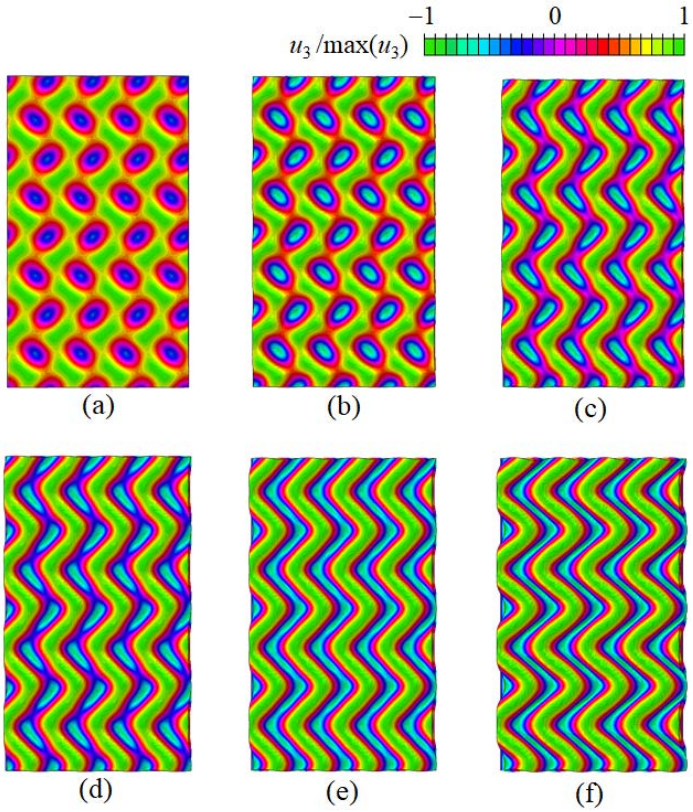


**Fig. 12.** Pattern evolution on the third bifurcated path analyzed using the imperfections of $\phi_{\mathrm{hex}}^{(1)} + \phi_{\mathrm{I}}^{(2)} + \phi_{\mathrm{I}}^{(3)}$ (Mode I). (a) $\mu/kT$=–0.54, (b) $\mu/kT$=–0.40, (c) $\mu/kT$=–0.36, (d) $\mu/kT$=–0.35, (e) $\mu/kT$=–0.30, and (f) $\mu/kT$=–0.20. The distorted dimples coalesce along the vertical direction such that a herringbone pattern appears. First, the hexagonal dimple pattern appears at the first bifurcation point. Second, the individual circular dimples are distorted at the second bifurcation point. The resulting pattern is similar to the uniaxial buckling mode that occurs in hexagonal honeycombs (Gibson and Asyby, 1997). Finally, the distorted dimples coalesce along the vertical direction at the third bifurcation to yield periodically arranged zigzag grooves (i.e., the herringbone pattern).

According to Chen and Hutchinson (2004), when the herringbone pattern is characterized by its width, $a$, breadth, $L$, and inclination angle, $\theta$, $a/h$=10, $L/h$=7.6, and $\theta$ =49° are easily obtained from the features of the first and second bifurcations, because $a/h$=10 and $L/h$=7.6 are determined by the dominant wavelengths of the sinusoidal wrinkle modes that occur at the first and second bifurcation points (Section 5), and $\theta$ =49°(=90°-41°) comes from the characteristic angle of the sinusoidal wrinkle mode at the second bifurcation (Appendices B and D). These values are considerably

consistent with the results obtained by Chen and Hutchinson (2004). Although Chen and Hutchinson (2004) considered the imperfections of the herringbone mode by parametrizing the values of $\theta$, $L$ and $\alpha$, we elucidated the evolution of the herringbone pattern caused by the first, second, and third bifurcations; that is, we determined that the herringbone pattern is not a bifurcation mode but a deformation pattern caused by the three sequential bifurcations. This finding answers the open question about the nature of the herringbone pattern posed by Chen and Hutchinson (2004). Moreover, our work reveals that the occurrence of the rectangular checkerboard modes in the three symmetric directions at the second bifurcation (Fig. 6) is the missing link in the evolution from the hexagonal dimple pattern to the herringbone pattern.

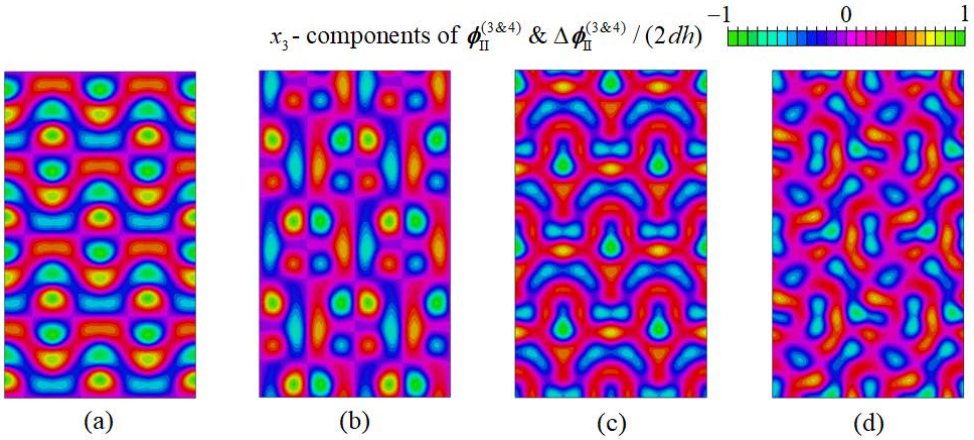


**Fig. 13.** The bifurcation modes at the third and fourth bifurcation points analyzed from Mode II and the imperfections used to analyze the third and fourth bifurcated paths. (a) $\boldsymbol{\phi}_{\mathrm{II}}^{(3)}$, (b) $\boldsymbol{\phi}_{\mathrm{II}}^{(4)}$, (c) $\boldsymbol{\phi}_{\mathrm{hex}}^{(1)}+\boldsymbol{\phi}_{\mathrm{II}}^{(2)}+\boldsymbol{\phi}_{\mathrm{II}}^{(3)}$, and (d) $\boldsymbol{\phi}_{\mathrm{hex}}^{(1)}+\boldsymbol{\phi}_{\mathrm{II}}^{(2)}+\boldsymbol{\phi}_{\mathrm{II}}^{(3)}+\boldsymbol{\phi}_{\mathrm{II}}^{(4)}$. The bifurcation points are $k_{\mathrm{II}}^{(3)}=k_{\mathrm{II}}^{(4)}=1$. Although the bifurcation modes cannot be used to predict the resulting deformation patterns, the imperfections imply the coalescence of the selected pairs of distorted dimples.

### *6.2. Pattern evolution from Modes II and III*

By analyzing the bifurcation point on the second bifurcated path generated by Mode II (Fig. 9d–f), the third bifurcation point and mode are obtained as $k_{\mathrm{II}}^{(3)}=1$ and $\boldsymbol{\phi}_{\mathrm{II}}^{(3)}$ (i.e., a single bifurcation). Further, the fourth bifurcation point and mode on the third bifurcated path are obtained as $k_{\mathrm{II}}^{(4)}=1$ and $\boldsymbol{\phi}_{\mathrm{II}}^{(4)}$. Fig. 13 shows the bifurcation modes, $\boldsymbol{\phi}_{\mathrm{II}}^{(3)}$ and $\boldsymbol{\phi}_{\mathrm{II}}^{(4)}$, and the respective imperfections, $\boldsymbol{\phi}_{\mathrm{hex}}^{(1)}+\boldsymbol{\phi}_{\mathrm{II}}^{(2)}+\boldsymbol{\phi}_{\mathrm{II}}^{(3)}$ and $\boldsymbol{\phi}_{\mathrm{hex}}^{(1)}+\boldsymbol{\phi}_{\mathrm{II}}^{(2)}+\boldsymbol{\phi}_{\mathrm{II}}^{(3)}+\boldsymbol{\phi}_{\mathrm{II}}^{(4)}$, which we use to trace the third and fourth bifurcated paths. Although the bifurcation modes (Fig. 13a,b) are complex and cannot be used to predict the resulting deformation patterns, the imperfections (Fig. 13c,d) can be used to predict

the coalescence of the selected pairs of the distorted dimples. This tendency of the bifurcations is confirmed by postbuckling analysis.

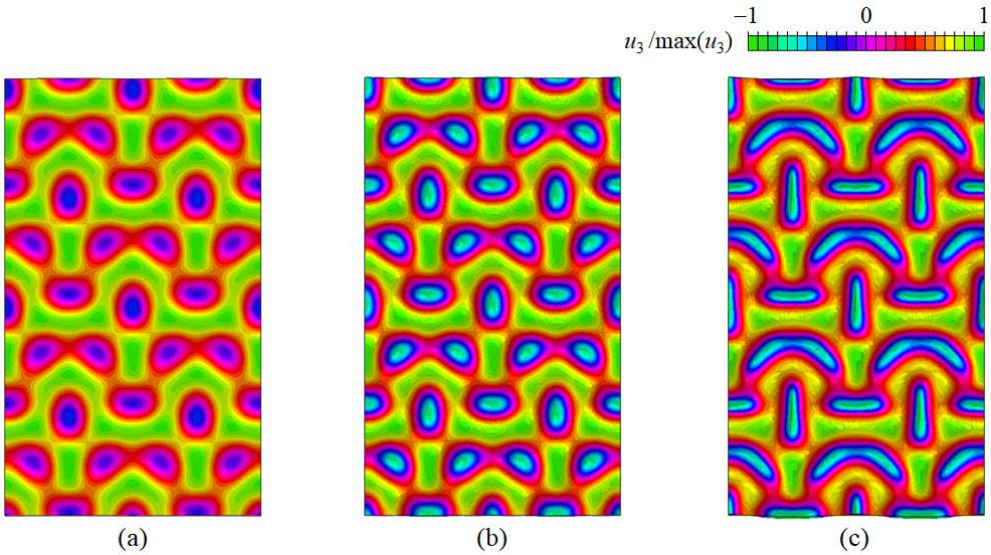


**Fig. 14.** Pattern evolution on the third bifurcated path analyzed using the imperfections of $\boldsymbol{\phi}_{\text{hex}}^{(1)}+\boldsymbol{\phi}_{\text{II}}^{(2)}+\boldsymbol{\phi}_{\text{II}}^{(3)}$ (Mode II). (a) $\mu/kT$=–0.54, (b) $\mu/kT$=–0.40, and (c) $\mu/kT$=–0.27. The deformation pattern from Mode II is caused by the coalescence of the two selected dimples neighboring those elongated in the vertical and horizontal directions, leading to the occurrence of arch-like grooves.

Fig. 14 shows the pattern evolution caused by $\boldsymbol{\phi}_{\text{hex}}^{(1)}+\boldsymbol{\phi}_{\text{II}}^{(2)}+\boldsymbol{\phi}_{\text{II}}^{(3)}$ on the third bifurcated path, and Fig. 15 shows the pattern evolution caused by $\boldsymbol{\phi}_{\text{hex}}^{(1)}+\boldsymbol{\phi}_{\text{II}}^{(2)}+\boldsymbol{\phi}_{\text{II}}^{(3)}+\boldsymbol{\phi}_{\text{II}}^{(4)}$ on the fourth bifurcated path. Figs. 14 and 15 demonstrate that the deformation patterns evolve with the coalescences of the dimples. Although the herringbone pattern from Mode I is caused by the coalescences of the all dimples aligned in the vertical direction, the deformation pattern from Mode II is caused by the coalescence of the two selected dimples on the third bifurcated path, leading to the occurrence of the arch-like grooves in Fig. 14. By contrast, on the fourth bifurcated path, the two dimples elongated in the vertical and horizontal directions and the one arch-like groove coalesce, leading to the formation of the periodic zigzag grooves in Fig. 15. This can be regarded as a periodical labyrinth pattern. Experimentally observed labyrinth patterns (Breid and Crosby, 2009,2011; Guvendiren et al., 2009,2010a,2010b) seem to form through the random arrangement of zigzag grooves.

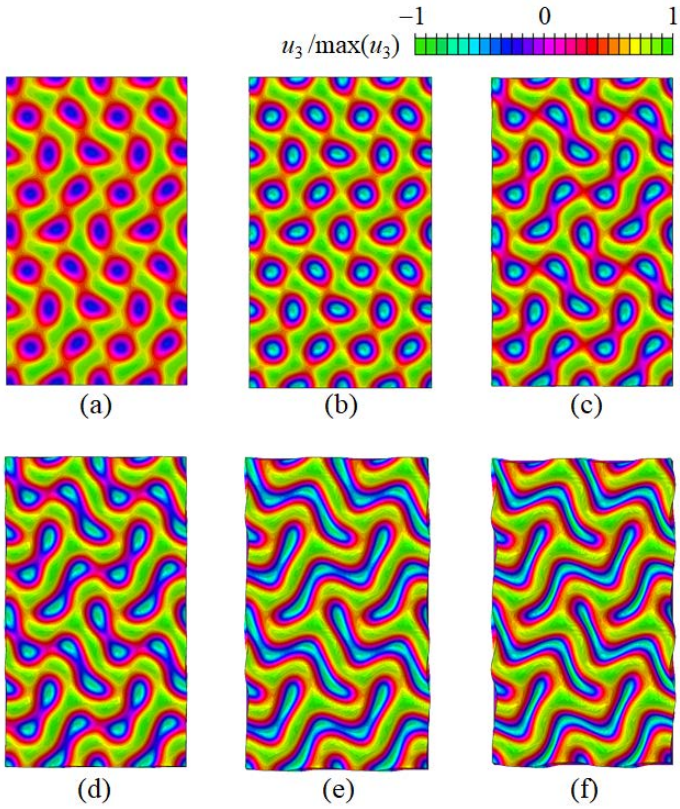


**Fig. 15.** Pattern evolution on the fourth bifurcated path analyzed using the imperfections of $\boldsymbol{\phi}_{\text{hex}}^{(1)} + \boldsymbol{\phi}_{\text{II}}^{(2)} + \boldsymbol{\phi}_{\text{II}}^{(3)} + \boldsymbol{\phi}_{\text{II}}^{(4)}$ (Mode II). (a) $\mu/kT$=–0.54, (b) $\mu/kT$=–0.44, (c) $\mu/kT$=–0.41, (d) $\mu/kT$=–0.40, (e) $\mu/kT$=–0.32, and (f) $\mu/kT$=–0.23. Arch-like grooves on the third bifurcated path coalesce with the two elongated dimples, leading to the formation of zigzag grooves. The deformation pattern is produced by the periodic arrangement of the zigzag grooves, which can be viewed as a periodical labyrinth pattern.

It should be noted that the distinct contribution of the third bifurcation in Fig. 14 becomes almost invisible after pattern evolution, as shown in Fig. 15. This is because the third and fourth bifurcations occur near each other, and in the postbuckling analysis, the bifurcation modes at the sequential bifurcation points are superposed and introduced as the initial imperfections (Section 3). Thus, the hierarchical structure of bifurcations may be invisible in the numerical analysis as well as in experiments. However, the post buckling analysis needs to detect the sequential bifurcation points and to obtain the individual bifurcation modes. The approach used in the present study (i.e., step-by-step eigenvalue buckling analysis; Section 3) is sufficiently powerful to be able to trace the evolutional process caused by sequential bifurcations.

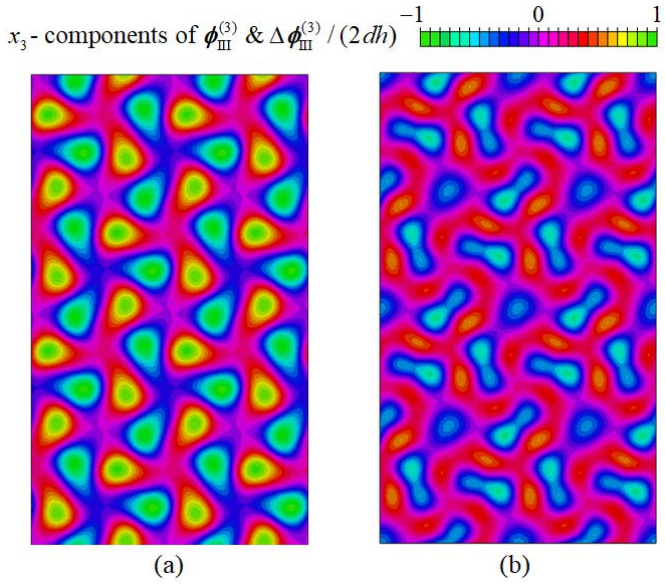


**Fig. 16.** The bifurcation mode at the third bifurcation point analyzed from Mode III and the imperfections used to analyze the third bifurcated path. (a) $\boldsymbol{\phi}_{\mathrm{III}}^{(3)}$ and (b) $\boldsymbol{\phi}_{\mathrm{hex}}^{(1)}+\boldsymbol{\phi}_{\mathrm{III}}^{(2)}+\boldsymbol{\phi}_{\mathrm{III}}^{(3)}$. The bifurcation point is $k_{\mathrm{III}}^{(3)}=1$. This bifurcation mode causes the selective coalescence of the three distorted dimples with the dimple at the center of the flower (Fig. 9).

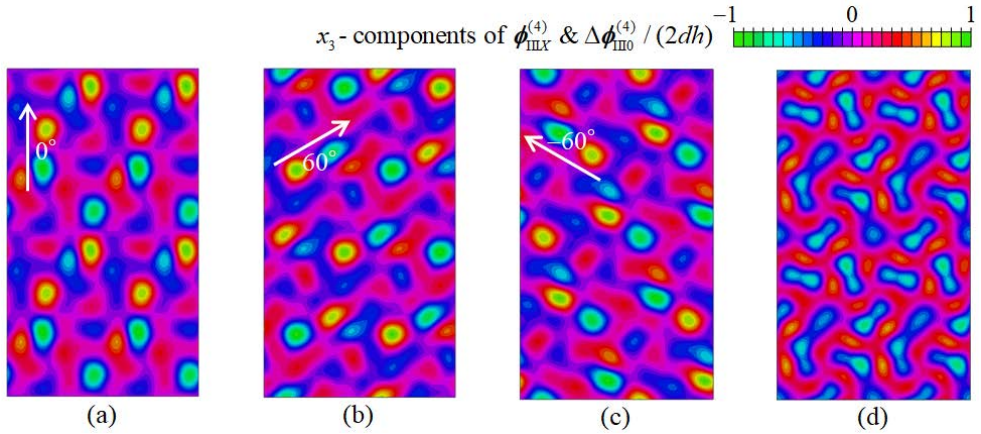


**Fig. 17.** The bifurcation modes at the fourth bifurcation point analyzed from Mode III and the imperfections used to analyze the fourth bifurcated path. (a) $\boldsymbol{\phi}_{\mathrm{III}0}^{(4)}$, (b) $\boldsymbol{\phi}_{\mathrm{III}60}^{(4)}$, (c) $\boldsymbol{\phi}_{\mathrm{III}60^*}^{(4)}$, and (d) $\boldsymbol{\phi}_{\mathrm{hex}}^{(1)}+\boldsymbol{\phi}_{\mathrm{III}}^{(2)}+\boldsymbol{\phi}_{\mathrm{III}}^{(3)}+\boldsymbol{\phi}_{\mathrm{III}0}^{(4)}$. The bifurcation point is $k_{\mathrm{III}}^{(4)}=3$, which produces $\boldsymbol{\phi}_{\mathrm{III}0}^{(4)}$, $\boldsymbol{\phi}_{\mathrm{III}60}^{(4)}$ and $\boldsymbol{\phi}_{\mathrm{III}60^*}^{(4)}$ as identical modes in the three symmetric directions with angles of 0° and $\pm 60°$. To avoid redundancy, we focus on the pathway generated using $\boldsymbol{\phi}_{\mathrm{hex}}^{(1)}+\boldsymbol{\phi}_{\mathrm{III}}^{(2)}+\boldsymbol{\phi}_{\mathrm{III}}^{(3)}+\boldsymbol{\phi}_{\mathrm{III}0}^{(4)}$.

When we analyze the bifurcation point on the second bifurcated path generated by Mode III (Fig. 9g–i), the third bifurcation point is found to occur with $k_{\mathrm{III}}^{(3)}=1$. Fig. 16 shows the bifurcation mode, $\boldsymbol{\phi}_{\mathrm{III}}^{(3)}$, and the imperfections, $\boldsymbol{\phi}_{\mathrm{hex}}^{(1)}+\boldsymbol{\phi}_{\mathrm{III}}^{(2)}+\boldsymbol{\phi}_{\mathrm{III}}^{(3)}$. This bifurcation mode can be viewed as a triangle mode (Cai et al., 2011), although it is slightly distorted. The imperfections (Fig. 16b) seem to cause the selective coalescence

of the three distorted dimples with the dimple at the center of the flower (Fig. 9). The fourth bifurcation point has the bifurcation modes, $\boldsymbol{\phi}_{\mathrm{III0}}^{(4)}$, $\boldsymbol{\phi}_{\mathrm{III60}}^{(4)}$ and $\boldsymbol{\phi}_{\mathrm{III60*}}^{(4)}$ (i.e., $k_{\mathrm{III}}^{(4)}$ =3). Fig. 17a–c shows that the three modes are the same bifurcation mode oriented in the symmetric directions with the angles of 0° and $\pm$60°, respectively. The directions are depicted by the arrows in the figure.

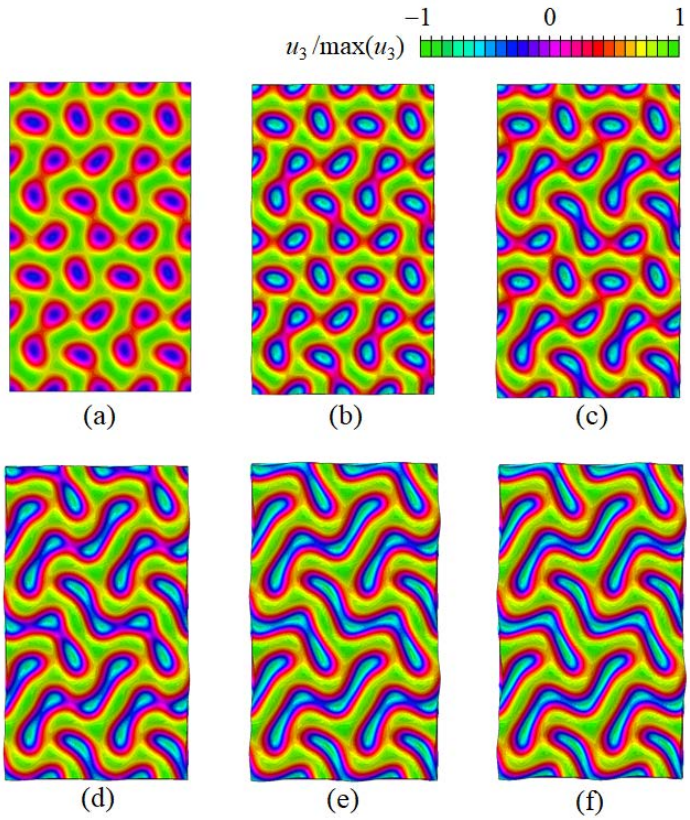


**Fig. 18.** Pattern evolution on the fourth bifurcated path analyzed using the imperfections of $\boldsymbol{\phi}_{\mathrm{hex}}^{(1)}+\boldsymbol{\phi}_{\mathrm{III}}^{(2)}+\boldsymbol{\phi}_{\mathrm{III}}^{(3)}+\boldsymbol{\phi}_{\mathrm{III0}}^{(4)}$ (Mode III). (a) $\mu/kT$=–0.54, (b) $\mu/kT$=–0.40, (c) $\mu/kT$=–0.39, (d) $\mu/kT$=–0.38, (e) $\mu/kT$=–0.33, and (f) $\mu/kT$=–0.30. Although the coalescence process is different to that for Mode II (Fig. 15), the resulting deformation pattern is periodically identical to that obtained by $\boldsymbol{\phi}_{\mathrm{hex}}^{(1)}+\boldsymbol{\phi}_{\mathrm{II}}^{(2)}+\boldsymbol{\phi}_{\mathrm{II}}^{(3)}+\boldsymbol{\phi}_{\mathrm{II}}^{(4)}$ (Mode II). Because $\boldsymbol{\phi}_{\mathrm{III0}}^{(4)}$ is only introduced into the imperfections as the fourth bifurcation mode, the hexagonal symmetry is lost. Therefore, the pattern evolution from Modes II and III yields identical deformation patterns, which can be interpreted as the periodic arrangement of the zigzag grooves resulting from the coalescence of four dimples (i.e., a periodical labyrinth pattern).

To avoid redundancy, we focus on the pathway generated using $\boldsymbol{\phi}_{\mathrm{hex}}^{(1)}+\boldsymbol{\phi}_{\mathrm{III}}^{(2)}+\boldsymbol{\phi}_{\mathrm{III}}^{(3)}+\boldsymbol{\phi}_{\mathrm{III0}}^{(4)}$ (Fig. 17d). Fig. 18 shows that, although the coalescence process is different to that for Mode II, the resulting deformation pattern is periodically equivalent to that generated by $\boldsymbol{\phi}_{\mathrm{hex}}^{(1)}+\boldsymbol{\phi}_{\mathrm{II}}^{(2)}+\boldsymbol{\phi}_{\mathrm{II}}^{(3)}+\boldsymbol{\phi}_{\mathrm{II}}^{(4)}$ from Mode II (Fig. 15). Because

$\boldsymbol{\phi}_{\mathrm{III0}}^{(4)}$ is introduced into the imperfections as the fourth bifurcation mode, the hexagonal symmetry is lost, such that the pattern evolution from Modes II and III yields the identical deformation patterns, consisting of the periodic arrangement of the zigzag grooves resulting from the coalescence of the four dimples (i.e., a periodical labyrinth pattern).

## 7. Conclusions

We investigated bifurcation and deformation during the evolution of periodic patterns on a gel film bonded to a soft substrate. The inhomogeneous field theory for polymeric gels was used in 3D finite element analysis (Section 2), while buckling and postbuckling analyses (Section 3) were performed during pattern evolution from the occurrence of the hexagonal dimple mode at the first bifurcation (Figs. 4 and 5). The new findings are described below.

The second bifurcation consisted of the rectangular checkerboard modes in three symmetric directions (i.e., $k^{(2)}$=3, a triple bifurcation) (Fig. 6). The rectangular checkerboard modes were explained well using the sinusoidal wrinkle modes categorized by $m$ and $n$ (i.e., $M$=12, a duodecuple bifurcation) (Figs. D.1 and D.2). The evolution of the hexagonal dimple pattern on the first bifurcated path allowed the three rectangular checkerboard modes to occur selectively ($M$=12 is reduced to $k^{(2)}$=3). The resulting deformation patterns on the second bifurcated paths were in good agreement with experiments (Breid and Crosby, 2009,2011), which, surprisingly, revealed an analogy with the in-plane buckling behavior of hexagonal honeycombs. The first bifurcation yielded a hexagonal dimple structure, whereas the second bifurcation produced the uniaxial, biaxial and equibiaxial (flower-like) patterns (Gibson and Ashby, 1997; Papka and Kyriakides, 1999; Ohno et al., 2002), which we referred to as Modes I, II, and III, and consisted of the periodic arrangement of distorted dimples (Fig. 9). Modes I, II, and III were produced by the combination of the three rectangular checkerboard modes (Figs. 7 and 8).

The third bifurcation on the second bifurcated path from Mode I resulted in the occurrence and evolution of the herringbone pattern (Fig. 12). The third bifurcation generated a single bifurcation mode that triggered the coalescence of the distorted dimples that were alternately arranged in the vertical direction (Fig. 11). The characteristic dimensions of the herringbone pattern were uniquely estimated using the

sinusoidal wrinkle modes categorized by *m* and *n*; that is, the ratio of the width and breadth was the ratio of the dominant wavelengths (i.e., 10 and 7.6), for the first and second bifurcations. In addition, the inclination angle was 49° (=90°–41°); this is the characteristic angle between the two sinusoidal wrinkle modes needed to express the resulting rectangular checkerboard mode. These dimensional values were consistent with those obtained by Chen and Hutchinson (2004). We determined that the herringbone pattern is not a bifurcation mode but a deformation pattern caused by the three sequential bifurcations. This finding answered the open question about the nature of the herringbone pattern posed by Chen and Hutchinson (2004).

The further bifurcations from Modes II and III led to the occurrence and evolution of a periodical labyrinth pattern (Figs. 15 and 18). The third and fourth bifurcations yielded zigzag grooves arising from the coalescence of four dimples. Modes II and III had different bifurcation modes (Figs. 13, 16 and 17), owing to the different coalescence processes, although the resulting deformation patterns were identical to the periodical labyrinth pattern formed by the periodic arrangement of zigzag grooves. We revealed that the occurrence of the rectangular checkerboard modes in the three symmetric directions at the second bifurcation (Fig. 6) is the missing link in the evolution from the hexagonal dimple pattern to the herringbone and labyrinth patterns.

Finally, it is fruitful to consider the key factors that cause the occurrence of the rectangular checkerboard modes at the second bifurcation, because the occurrence may depend on inhomogeneous gel swelling (Section 2) and/or the successful detection of the second bifurcation may be critical in eigenvalue buckling analysis (Section 3). Further, the ratio of the Young's moduli of the film and soft substrate may also be important, and the response may depend on the selection of constitutive models. In addition, the effect of the initial curvature of the film should be also significant (Cai et al., 2011; Zhao et al., 2019). These factors are considered to affect transient states during the pattern evolutions because in experiments, the pattern evolution is terminated by the formation of the herringbone/labyrinth patterns at the final stage. These questions are still open and should be addressed because the present study was focused on analyzing a specific set of a gel film on a soft substrate without parametric studies.

An exciting and challenging future research direction would be to investigate the bifurcations and evolution of more realistic labyrinth patterns than the periodical labyrinth pattern. Another challenge would be to analyze the convoluted shape of the human cerebral cortex induced by growth (Tallinen et al., 2014,2016; Zhao et al., 2019), which is considered to have a hierarchical structure with the complex interactions of creases and holds (Diab et al., 2013). To reduce computational costs, more sophisticated finite element analysis is needed. This could be achieved by introducing shell elements instead of solid elements (Xu et al., 2014) and/or artificial damping to solve smoothly the unstable problem with self-contact of films (Cao and Hutchinson, 2012; Okumura et al., 2015). The group-theoretic methods could also play an important role in reducing the computational costs (Healey, 1988).

**Declaration of competing interest**

The authors declare that they have no known competing financial interests or personal relationships that could have appeared to influence the work reported in this paper.

**Acknowledgments**

This work was partially supported by the Japan Society for the Promotion of Science (JSPS) under a Grant-in-Aid for Scientific Research (A) (JP19H00739). We thank Dr. Shingo Ozaki at Yokohama National University for sharing a reference on bifurcation analysis. We also thank Adam Brotchie, PhD, from Edanz Group (www.edanzediting.com/ac) for editing a draft of this manuscript.

**Appendix A. Eigenvalue buckling analysis in Abaqus**

This appendix is devoted to a brief explanation of the eigenvalue buckling analysis provided as the BUCKLE option in Abaqus (Abaqus 6.14; Bertoldi et al., 2008). First, we assume that an achieved base configuration is known by stresses $\sigma_{ij}^{\mathrm{b}}$ in equilibrium with surface traction $t_i^{\mathrm{b}}$ and body forces $q_i^{\mathrm{b}}$. From this base state, we consider an elastic deformation with small displacement gradients under additional surface tractions $\Delta t_i$, body forces $\Delta q_i$, and boundary displacements $\Delta u_i$. Such a deformation is a linear perturbation on the base state. Thus, if $\Delta\sigma_{ij}$ is the stress response to the loads $\Delta t_i$, $\Delta q_i$, and $\Delta u_i$, $\lambda\Delta\sigma_{ij}$ is the stress response for loads $\lambda\Delta t_i$, $\lambda\Delta q_i$, and $\lambda\Delta u_i$.

Individual distinct values of $\lambda$ correspond to a linear perturbation of the base state. Among these perturbed states, we seek special values of $\lambda$ that allow for the existence of nontrivial incremental displacement fields, which are referred to as buckling modes. In the eigenvalue buckling analysis in Abaqus, we do not distinguish between the geometry of the base state and the linearly perturbed configurations. This assumption allows us to seek the buckling modes as incremental displacements out of the base state geometry with stresses $\sigma_{ij}^{\mathrm{b}} + \lambda \Delta \sigma_{ij}$, applied tractions $t_i^{\mathrm{b}} + \lambda \Delta t_i$, and applied body forces $q_i^{\mathrm{b}} + \lambda \Delta q_i$.

To obtain Eq. (11) in Section 3, we consider the virtual work principle in terms of the nominal stress $P_{ij}$ in the base state. When $t_i$ is the nominal traction on the boundary in the base state and $q_i$ represents the body force per unit volume in the base state, the rate form of the virtual work principle is expressed as

$$\int_V \dot{P}_{ij} \frac{\partial \delta v_i}{\partial X_j} dV = \int_A \dot{t}_i \delta v_i dA + \int_V \dot{q}_i \delta v_i dV \,, \tag{A.1}$$

where $\delta v_i$ is an arbitrary virtual velocity field.

Since we have assumed that the base state and the current state (due to linearly perturbed configurations) are indistinguishable, the introduction of the Kirchhoff stress $\tau_{ij}$ and the velocity gradient $L_{ij}$ transforms the left-hand side of Eq. (A.1) into

$$\int_V \dot{P}_{ij} \frac{\partial \delta v_i}{\partial X_j} dV = \int_V \left\{ \mathring{\tau}_{ij} \delta D_{ij} + \tau_{ij} (\delta L_{ki} L_{kj} - 2 D_{ik} \delta D_{kj}) \right\} dV \,, \tag{A.2}$$

where $\mathring{\tau}_{ij}$ is the Jaumann rate of $\tau_{ij}$, $D_{ij}$ is the symmetric part of $L_{ij}$, and $\delta L_{ij}$ and $\delta D_{ij}$ are the arbitrary variations of $L_{ij}$ and $D_{ij}$, respectively. Eq, (A.2) is derived from the relations of $P_{ij} = \tau_{ik} F_{jk}^{-1}$, $\dot{F}_{ij} = L_{ik} F_{kj}$, and $\mathring{\tau}_{ij} = \dot{\tau}_{ij} - W_{ik} \tau_{kj} + \tau_{ik} W_{kj}$, where $F_{ij}$ is the deformation gradient, $L_{ij} = D_{ij} = (L_{ij} + L_{ji})/2$, and $W_{ij} = (L_{ij} - L_{ji})/2$. In addition, we can replace the kirchhoff stress $\tau_{ij}$ with the Cauchy stress $\sigma_{ij}$ since the base and current configurations are indistinguishable.

For the right-hand side of Eq. (A.1), it is assumed that the magnitude of the applied tractions and body forces is fixed and the change of their intensities arises due to the change in geometry. Thus, $\dot{t}_i$ and $\dot{q}_i$ depend only on the deformation gradient, that is,

$$\begin{cases} \dot{t}_i = \dfrac{\partial t_i}{\partial F_{jk}} \dot{F}_{jk} = \dfrac{\partial t_i}{\partial F_{jk}} L_{jk} \\ \dot{q}_i = \dfrac{\partial q_i}{\partial F_{jk}} \dot{F}_{jk} = \dfrac{\partial q_i}{\partial F_{jk}} L_{jk} \end{cases} . \tag{A.3}$$

Assuming a hypoelastic constitutive law,

$$\overset{\circ}{\tau}_{ij} = C_{ijkl}(\boldsymbol{\sigma}) D_{kl} , \tag{A.4}$$

where $C_{ijkl}(\boldsymbol{\sigma})$ can depend on the current stress.

When Eqs. (A.2)–(A.4) are substituted into Eq. (A.1), the current state described as $\sigma_{ij}^{\mathrm{b}} + \lambda \Delta\sigma_{ij}$, $t_i^{\mathrm{b}} + \lambda \Delta t_i$, and $q_i^{\mathrm{b}} + \lambda \Delta q_i$ leads to

$$\begin{aligned} &\int_V \delta D_{ij} C_{ijkl}(\boldsymbol{\sigma}^{\mathrm{b}}) D_{kl} dV + \int_V (\sigma_{ij}^{\mathrm{b}} + \lambda \Delta\sigma_{ij})(\delta L_{ki} L_{kj} - 2 D_{ik} \delta D_{kj}) dV \\ &\quad - \int_A \delta v_i \frac{\partial (t_i^{\mathrm{b}} + \lambda \Delta t_i)}{\partial F_{jk}} L_{jk} dA - \int_V \delta v_i \frac{\partial (q_i^{\mathrm{b}} + \lambda \Delta q_i)}{\partial F_{jk}} L_{jk} dV = 0 \end{aligned} . \tag{A.5}$$

Using the standard finite element approach, the finite element discretization of Eq. (A.5) results in Eq. (11), i.e.,

$$\{\mathbf{K}_0(\mathbf{P}) + \lambda_i \mathbf{K}_\Delta(\mathbf{P}, \mathbf{Q})\} \boldsymbol{\phi}_i = \mathbf{0} ,$$

where the generalized nodal forces resulting from both $t_i^{\mathrm{b}}$ and $q_i^{\mathrm{b}}$ as well as prescribed displacements $u_i^{\mathrm{b}}$ are denoted by **P** and those due to $\Delta t_i$, $\Delta q_i$, and $\Delta u_i$ are denoted by **Q**. Thus, the base state stiffness $\mathbf{K}_0(\mathbf{P})$ includes the effects of preloads acting in the base state. By contrast, the differential stiffness $\mathbf{K}_\Delta(\mathbf{P},\mathbf{Q})$ is derived from a linear perturbation on the base state, so that it includes the effects of incremental loads added at the base state. The eigenvalues $\lambda_i$ present the multipliers of the incremental

loads (i.e., **Q**) to predict the generalized critical buckling loads as $\mathbf{P}+\lambda_i\mathbf{Q}$, while the corresponding eigenvectors $\boldsymbol{\phi}_i$ give the associated buckling modes.

## Appendix B. Sinusoidal wrinkle modes depending on $L_1$ and $L_2$

Fig. B.1 shows that the wavelength, $\lambda$, and the wave direction, $\xi$, of sinusoidal wrinkle modes are restricted to the dimensions of $L_1$ and $L_2$ because of the assumption of the periodic arrangement of the unit cells. A combination of $m$ and $n$ is chosen for the wave numbers in the $x_1$- and $x_2$- directions, respectively. A potential wrinkle mode discretized by $m$ and $n$ has a wave direction identified by the angle, $\psi$, given by

$$\tan\psi = \frac{L_2/n}{L_1/m}, \tag{B.1}$$

and a wavelength of

$$\lambda = \frac{L_1 L_2}{\sqrt{L_1^2 n^2 + L_2^2 m^2}}. \tag{B.2}$$

The sinusoidal wrinkle modes can simply be expressed as

$$\alpha_\xi \sin\left(\frac{2\pi\xi}{\lambda}\right) + \beta_\xi \cos\left(\frac{2\pi\xi}{\lambda}\right), \tag{B.3}$$

where $\alpha_\xi$ and $\beta_\xi$ are coefficients to allow an arbitrary phase shift. Thus, the corresponding mode identified by $m$ and $n$ appears as a double bifurcation (i.e., $M$=2) (Okumura et al., 2004), where $M$ is defined as the multiplicity of bifurcations. In addition, the counterpart of Eq. (B.3) also appears in the opposite direction, $\xi^*$, because of symmetry (Fig. B.1), although the counterpart is absent in the cases of $m$=0 or $n$=0 because $\psi$=0° or 90°. Thus, the set of the individual modes with $m$=0 or $n$=0 occurs as a double bifurcation ($M$=2), whereas the modes without $m$=0 and $n$=0 occur as a quadruple bifurcation ($M$=4).

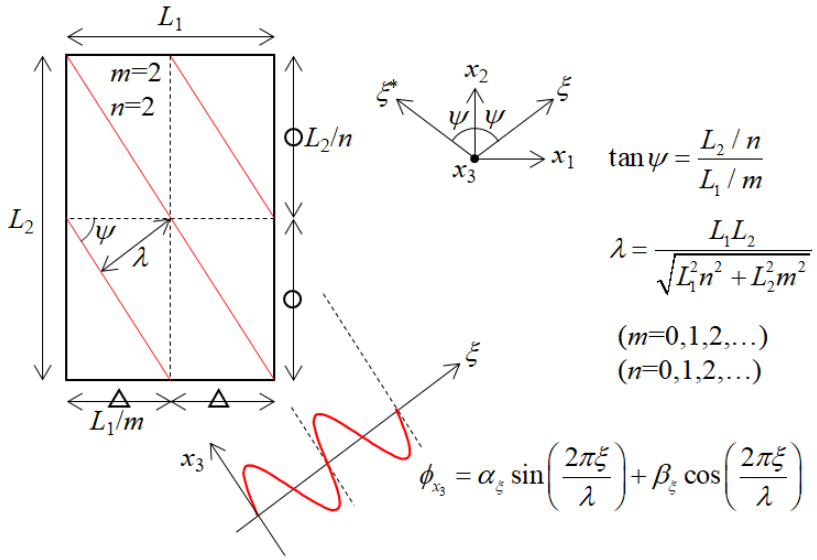


**Fig. B.1.** Sinusoidal wrinkle modes restricted to the dimensions of the unit cell. The wavelength, $\lambda$, and the direction, $\xi$, identified by the angle, $\psi$, depend on the ratio of $L_1$ and $L_2$. A combination of $m$ and $n$ is chosen from $m$=0,1,2,… and $n$=0,1,2,… although only the case of $m$=$n$=2 is depicted as an example. The potential modes discretized by $m$ and $n$ appear as a double bifurcation ($M$=2) because the phase is arbitrarily determined by the coefficients, $\alpha_\xi$ and $\beta_\xi$(Okumura et al., 2004). In addition, the counterpart mode also appears in the oppisite direction, $\xi^*$, because of symmetry. Thus, the modes without $m$=0 and $n$=0 occur as a quadruple bifurcation ($M$=4).

To focus on the hexagonal dimple mode, we consider the case of $L_2/L_1=\sqrt{3}$; in this case, Eqs. (B.1) and (B.2) reduce to

$$\tan\psi = \frac{\sqrt{3}m}{n}, \tag{B.4}$$

$$\lambda = \frac{L_2}{\sqrt{n^2 + 3m^2}}. \tag{B.5}$$

Table B.1 shows the properties of the representative wrinkle modes obtained from the unit cell with $L_2/L_1=\sqrt{3}$. Because the hexagonal dimple mode consists of the superposition of sinusoidal wrinkle modes in the three symmetric directions prescribed by the angles of 0° , +60°, and –60° (Audoly and Boudaund, 2008a; Cai et al., 2011), the combination of the modes discretized by ($m$, $n$)=(0, 2) and ($m$, $n$)=(1, 1) is found to produce the hexagonal dimple mode. In the present study, we recognize the hexagonal dimple mode as $M$=2+4=6 (i.e., a sextuple bifurcation) and $\lambda/L_2$ =0.5. The sinusoidal

wrinkle mode with the dominant wavelength, $\lambda_{cr}$, occurs at the first bifurcation on the primary path (Chen and Hutchinson, 2004). To analyze the occurrence of the hexagonal dimple mode at the first bifurcation, the value of $0.5L_2$ must be adjusted to be $\lambda_{cr}=0.5L_2$. Because the critical length of $L_2$ with $\lambda_{cr}=0.5L_2$ is unknown for gel films (cf. Chen and Hutchinson, 2004), step-by-step eigenvalue buckling analysis (Section 3) is performed by parametrizing the value of $L_2$ (Appendix C).

**Table B.1.** Sets of the angle, $\psi$, wavelength, $\lambda$, and multiplicity of bifurcations, $M$, obtained from the representative set of $m$ and $n$ with $L_2/L_1=\sqrt{3}$. The hexagonal dimple mode consist of the combination of the modes categorized by ($m$, $n$)=(0, 2) and ($m$, $n$)=(1, 1). The angles between the individual directions are 60° and the wavelength is $0.5L_2$. The corresponding bifurcation point is recognized as $M$=2+4=6.

| $m$ | $n$ | $\psi$ | $\lambda/L_2$ | $M$ |
|---|---|---|---|---|
| 0 | 1 | 0° | 1 | 2 |
| 1 | 0 | 90° | 0.58 | 2 |
| 0 | 2 | 0° | 0.5 | 2 |
| 1 | 1 | 60° | 0.5 | 4 |
| 1 | 2 | 41° | 0.38 | 4 |
| 0 | 3 | 0° | 0.33 | 2 |

## Appendix C. Dominant wavelength at the first bifurcation

Fig. C.1 shows the first bifurcation points detected on the primary path, which depend on the value of $L_2/h$=14,16,18,20,22, and 24 of the unit cell, because the critical wavelength is restricted to the combination of $L_2/h$ and the wave property discretized by $m$ and $n$ (Appendix B). We set $\Delta\mu/kT=0.01$ as the increments of $\mu_b/kT$. When $\mu_b/kT=-0.53$ is used for $L_2/h$=16,18,20, and 22, the Abaqus analysis provides a message that the point is already beyond a bifurcation point. Thus, the critical value for the first bifurcation is taken as $\mu_{cr}/kT=\mu_b/kT=-0.54$. To produce the hexagonal dimple mode, the critical length of $L_2$ with $\lambda_{cr}=0.5L_2$ is needed, which can be found in the unit cells of $L_2/h$=16,18,20, and 22.

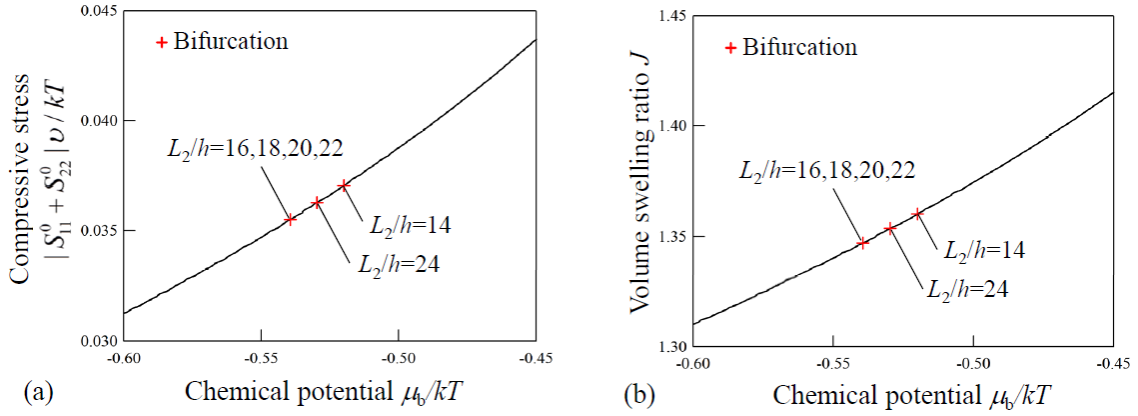


**Fig. C.1.** The first bifurcation points on the primary path for different values of $L_2/h$=14,16,18,20,22, and 24. (a) In-plane compressive stress, $\left|S_{11}^0+S_{22}^0\right|\upsilon/kT$, and (b) volume swelling ratio, $J$. The critical value for the first bifurcation is $\mu_{cr}/kT=\mu_b/kT=-0.54$. The critical length of $L_2$ with $\lambda_{cr}=0.5L_2$ can be found in the unit cells of $L_2/h$=16,18,20, and 22. Here, $\left|S_{11}^0+S_{22}^0\right|_{cr}\upsilon/kT$ =0.0355 and $J_{cr}$=1.34.

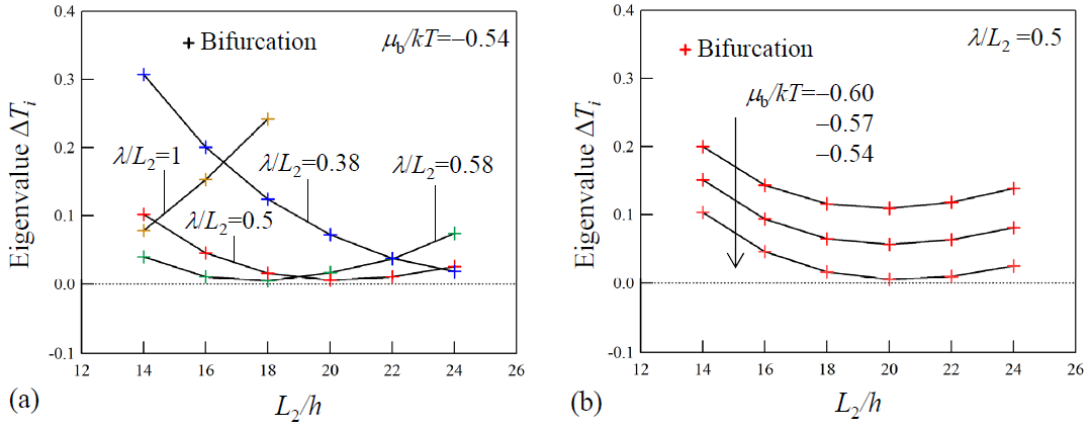


**Fig. C.2.** Relationships between $\Delta\theta_i$, $\lambda/L_2$ and $L_2/h$. (a) Wavelengths categorized using $\lambda/L_2$=1, 0.58, 0.5 and 0.38 at $\mu_b/kT$=–0.54 and (b) the change in eigenvalues for $\lambda/L_2$=0.5 for different values of $\mu_b/kT$. The minimum eigenvalue is approximately zero at $\mu_{cr}/kT$ =–0.54 in the two cases of $L_2/h$=18 and 20. When $L_2/h$=20 is selected, the hexagonal dimple mode appears with a critical wavelength of $\lambda_{cr}/h$=0.5×20=10. By contrast, when $L_2/h$=18 is assumed, a stripe mode in the horizontal direction appears with a critical wavelength of $\lambda_{cr}/h$=0.58×18=10.4.

Fig. C.2 shows the relationships between the eigenvalues, $\Delta\theta_i$, and the values of $\lambda/L_2$ as a function of $L_2/h$. Fig. C.2a shows that the minimum eigenvalue is approximately zero at $\mu_{cr}/kT$ =–0.54 in the two cases of $L_2/h$=18 and 20, which have the wavelengths of $\lambda/L_2$=0.58 and 0.5, respectively. The other eigenvalues belong to $\lambda/L_2$=1, 0.58, 0.5, and 0.38. The individual wavelengths correspond to multiplicity of bifurcations of $M$=2, 2, 6, and 4, respectively (Table B.1). This categorization is verified by checking the individual buckling modes. Fig. C.2b shows the decrease of the

eigenvalues with $\lambda/L_2$=0.5 as the value of $\mu/kT$ increases from –0.60 to –0.54. As discussed in Appendix B, the hexagonal dimple mode appears with $\lambda/L_2$=0.5. When $L_2/h$=20 is selected, the hexagonal dimple mode has a critical wavelength of $\lambda_{cr}$=0.5$L_2$ (i.e., $\lambda_{cr}/h$=0.5×20=10). By contrast, if $L_2/h$=18 is assumed (Table B.1) the sinusoidal wrinkle mode has a critical wavelength of $\lambda_{cr}/h$=0.58×18=10.4, and the corresponding mode is the stripe mode in the horizontal direction because $M$=2 and $\psi$=90°.

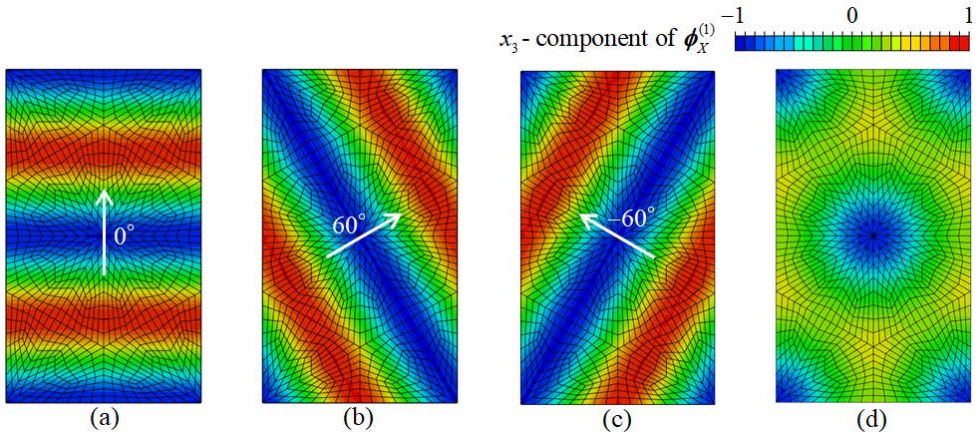


**Fig. C.3.** Dominant bifurcation modes at the first bifurcation point on the primary path for $\lambda/L_2$=0.5 ($M$=6) with $L_2/h$=20. (a) $\phi_0^{(1)}$, (b) $\phi_{60}^{(1)}$, (c) $\phi_{60^*}^{(1)}$, and (d) $\phi_{hex}^{(1)}=\phi_0^{(1)}+\phi_{60}^{(1)}+\phi_{60^*}^{(1)}$. To obtain the unique hexagonal dimple mode as $\phi_{hex}^{(1)}=\phi_0^{(1)}+\phi_{60}^{(1)}+\phi_{60^*}^{(1)}$, $\phi_0^{(1)}$, $\phi_{60}^{(1)}$, and $\phi_{60^*}^{(1)}$ are obtained by controlling the individual phase shifts to assign one dimple at the center of the unit cell.

The critical wavelengths are estimated to be in the range of $\lambda_{cr}/h$=10~10.4. In the present study, we focus on the occurrence of the hexagonal dimple mode (Fig. C.3). Thus, $L_2/h$=20 is used to analyze pattern evolution from the hexagonal dimple mode with $\lambda_{cr}/h$=10 (Section 5). We note that this study did not focus on precisely determining the unique dominant wavelength. This is to avoid the high computational costs of performing analyses using small values of $\Delta\mu/kT$. Further, intermediate values between the values of $L_2/h$ are chosen as integer values. Although the theoretical value is $\lambda_{th}/h$=8.1 from $\lambda_{th}/h=2\pi(E_f/3E_s)^{1/3}$ with $E_f/E_s$ =6.5 (Section 4), the obtained values of $\lambda_{cr}/h$=10~10.4 can be considered to be reasonable, as detailed below. At the critical point of $\mu_{cr}/kT$ =–0.54, the thickness of the film, $h^*$, is increased because of swelling from the initial thickness, $h$. This change is estimated as $h^*$=1.34$h$ because $J_{cr}$=1.34 (Fig. C.1b). When $h^*$ is introduced as $\lambda_{th}/h^*=2\pi(E_f/3E_s)^{1/3}$, the reduced nominal value

(DuPont et al., 2010) yields $\lambda_{th}/h$=1.34×8.1=10.8, which provides good agreement with $\lambda_{cr}/h$=10~10.4, despite ignoring the material nonlinearities of the film and substrate.

Fig. C.3a–c shows the three bifurcation modes, $\boldsymbol{\phi}_0^{(1)}$, $\boldsymbol{\phi}_{60}^{(1)}$, and $\boldsymbol{\phi}_{60^*}^{(1)}$, analyzed for $L_2/h$=20 at $\mu_{cr}/kT$ =–0.54. Because $\lambda/L_2$=0.5 is accompanied by $M$=6=$k^{(1)}$, the sinusoidal wrinkle modes in the three symmetric directions has arbitrary phase shifts (Appendix B). To obtain the unique hexagonal dimple mode, $\boldsymbol{\phi}_{hex}^{(1)}$ (Fig. C.3d), $\boldsymbol{\phi}_0^{(1)}$, $\boldsymbol{\phi}_{60}^{(1)}$, and $\boldsymbol{\phi}_{60^*}^{(1)}$ are analyzed by controlling the individual phase shifts to assign one dimple at the center of the unit cell. Thus, $\boldsymbol{\phi}_{hex}^{(1)}$ is obtained as $\boldsymbol{\phi}_{hex}^{(1)} = \boldsymbol{\phi}_0^{(1)} + \boldsymbol{\phi}_{60}^{(1)} + \boldsymbol{\phi}_{60^*}^{(1)}$

**Appendix D. Interpretation of the second bifurcation modes**

To interpret the occurrence of rectangular checkerboard modes in the three symmetric directions at the second bifurcation point (Section 5), the sinusoidal wrinkle modes discretized by $m$ and $n$ are considered again (Appendix B). The case of $L_2/L_1$= $\sqrt{3}$ is fixed, which allows us to use Eqs. (B.4) and (B.5). When the values of $m$ and $n$ are parametrized to explore the wave properties, the combination of ($m$, $n$)=(2, 10), ($m$, $n$)=(4, 8) and ($m$, $n$)=(6, 2) gives a reasonable explanation of the occurrence of the rectangular checkerboard modes in the three symmetric directions (Table D.1). The reduced combination of ($m$, $n$)=(1, 5), ($m$, $n$)=(2, 4) and($m$, $n$)=(3, 1) also gives the same explanation if $L_2/h$=40 is considered instead of $L_2/h$=80. This specific combination yields $M$=4+4+4=12 (i.e., a duodecuple bifurcation). For $L_2/h$=80, we analyze the second bifurcation modes using the combination of ($m$, $n$)=(2, 10), ($m$, $n$)=(4, 8), and ($m$, $n$)=(6, 2).

Table D.1 shows the wave properties described by the combination of ($m$, $n$)=(2, 10), ($m$, $n$)=(4, 8) and ($m$, $n$)=(6, 2) (i.e., $\lambda/L_2$=0.095). The resulting sinusoidal wrinkle modes have individual directions characterized by $\psi = \pm 19°$, $\pm 41°$ and $\pm 79°$(=$\mp$ 101°), respectively (Fig. D.1). The wrinkle modes are not orthogonal to each other; thus, the superposition of the two selected wrinkle modes yields a rectangular checkerboard mode. Fig. D.2 shows the rectangular checkerboard modes obtained from superposing the two wrinkle modes prescribed by the set of $\pm 41°$, 19° and –79°(=101°), and –19° and 79°(=–101°), respectively. Fig. D.2 demonstrates that they correspond to the

checkerboard modes, $\boldsymbol{\phi}_{\mathrm{cb0}}$, $\boldsymbol{\phi}_{\mathrm{cb60}}$, and $\boldsymbol{\phi}_{\mathrm{cb60*}}$, predicted by the eigenvalue buckling analysis (Fig. 6). These representative directions characterized by the angles of 0° and ±60°, are confirmed as 0°=(41°–41°)/2 and ±60°=±(19°+101°)/2, respectively (Fig. 6a–c). Thus, the individual wavelengths are defined as $\lambda/h$=7.6 (=0.095×80). In addition, when $L_2/h$=40 is considered, the same bifurcation behavior as for $\lambda/h$=7.6 (=0.190×40) occurs for the combination of ($m$, $n$)=(1, 5), ($m$, $n$)=(2, 4) and($m$, $n$)=(3, 1) (Table D.1).

**Table D.1.** Sets of the angle, $\psi$, wavelength, $\lambda$, and multiplicity of bifurcations, $M$, obtained from the specific sets of $m$ and $n$ with $L_2/L_1=\sqrt{3}$. The combination of ($m$, $n$)=(2, 10), ($m$, $n$)=(4, 8) and ($m$, $n$)=(6, 2) yields $M$=4+4+4=12 with $\lambda/L_2$=0.095, such that $L_2/h$=80 gives $\lambda/h$=7.6. When $L_2/h$=40 is considered, $\lambda/L_2$=0.190 results in $\lambda/h$=7.6.

| $m$ | $n$ | $\psi$ | $\lambda/L_2$ | $M$ |
|---|---|---|---|---|
| 1 | 5 | 19° | 0.190 | 4 |
| 2 | 4 | 41° | 0.190 | 4 |
| 3 | 1 | 79°(=–101°) | 0.190 | 4 |
| 2 | 10 | 19° | 0.095 | 4 |
| 4 | 8 | 41° | 0.095 | 4 |
| 6 | 2 | 79°(=–101°) | 0.095 | 4 |

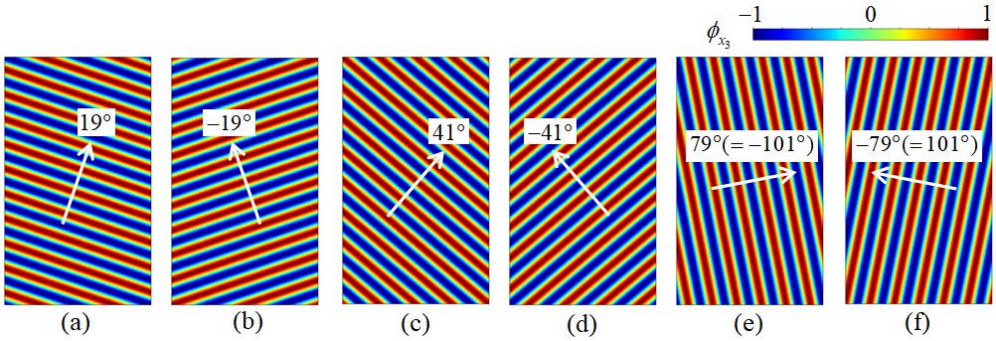


**Fig. D.1.** Six sinusoidal wrinkle modes described by ($m$, $n$)=(2, 10), ($m$, $n$)=(4, 8), and ($m$, $n$)=(6, 2): (a) $\psi$=19°, (b) $\psi$=–19°, (c) $\psi$=41°, (d) $\psi$=–41°, (e) $\psi$=79°(=–101°), and (f) $\psi$=–79°(=101°). We do not focus on the phase shift of the individual modes (Eq. (B.3)) because the rectangular checkerboard modes consisting of two wrinkle modes is periodically equivalent and independent of the phase shift.

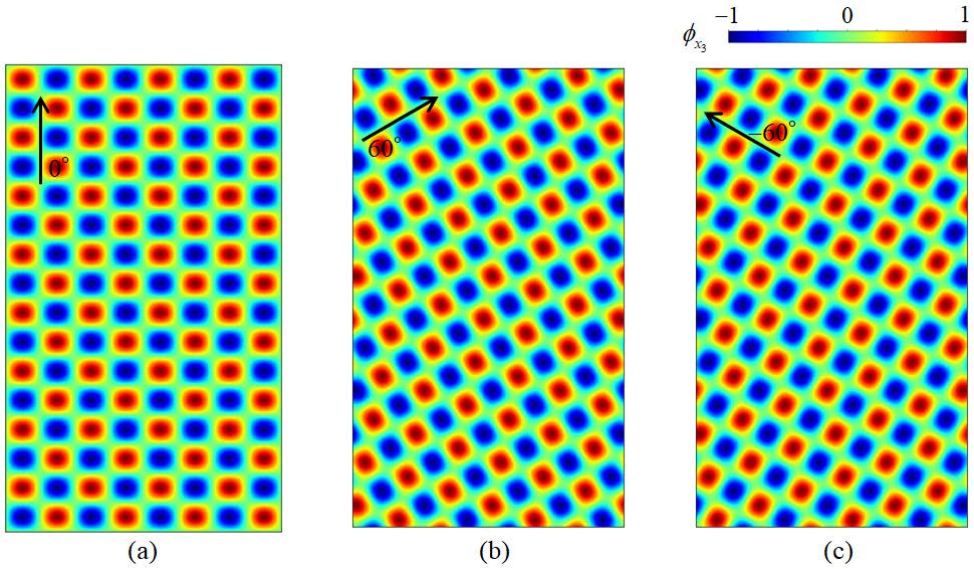


**Fig. D.2.** Rectangular checkerboard modes corresponding to $\boldsymbol{\phi}_{\mathrm{cb0}}^{(2)}$, $\boldsymbol{\phi}_{\mathrm{cb60}}^{(2)}$, and $\boldsymbol{\phi}_{\mathrm{cb60*}}^{(2)}$, obtained by superposing the two wrinkles prescribed by the set of (a) $\pm 41°$, (b) 19° and −79°(=101°), and (c) −19° and 79°(=−101°). These representative directions are characterized by the angles of 0° and $\pm 60°$ as 0°=(41°−41°)/2 and $\pm 60°=\pm$(19°+101°)/2, respectively.

We now address the question of why the three rectangular checkerboard modes, $\boldsymbol{\phi}_{\mathrm{cb0}}$, $\boldsymbol{\phi}_{\mathrm{cb60}}$, and $\boldsymbol{\phi}_{\mathrm{cb60*}}$ (Fig. D.2), are selected at the second bifurcation from a lot of potential modes generated from the six wrinkle modes in the characteristic directions (Fig. D.1). Because $M$=12, the six wrinkle modes also have the arbitrary phase shift (Appendix B). If several checkerboard modes are further superposed, $M$=12 provides a huge number of the potential modes, while $k^{(2)}$=3 at the second bifurcation provides only $\boldsymbol{\phi}_{\mathrm{cb0}}$, $\boldsymbol{\phi}_{\mathrm{cb60}}$ and $\boldsymbol{\phi}_{\mathrm{cb60*}}$. That is because at the second bifurcation point, the flat gel film on the primary path has already been deformed by the hexagonal dimple mode occurring at the first bifurcation point. Most of potential modes are not allowed to occur freely. We consider $M$=12 to be reduced to $k^{(2)}$=3 to maintain the symmetry of the hexagonal dimple mode; that is, $\boldsymbol{\phi}_{\mathrm{cb0}}^{(2)}$, $\boldsymbol{\phi}_{\mathrm{cb60}}^{(2)}$, and $\boldsymbol{\phi}_{\mathrm{cb60*}}^{(2)}$ are allowed to occur selectively as the dominant modes at the second bifurcation point.

It is finally noted that although Appendices B and D have been constructed based on intuition and experience, more sophisticated and systematic explanations may be derived from group-theoretic methods (Golbitsky et al., 1988; Ikeda and Murota, 2002). In addition, the present study showed that the film/substrate system is simple but its bifurcation behavior is incredibly rich and complicated. As described by Healey (1988),

the utilization of the group-theoretic approach to computational bifurcation analysis can lead to a dramatic reduction in numerical effort and enable the accurate computation of symmetry-breaking bifurcation points.

**References**


Abaqus 6.14 User Documentation, 2014. Dassault Systems SIMULIA Corporation.

Allen, H.G., 1969. In: Analysis and Design of Sandwich Panels. Pergamon Press, New York.

Audoly, B., Boudaoud, A., 2008a. Buckling of a thin film bound to a compliant substrate—Part I: formulation, linear stability of cylindrical patterns, secondary bifurcations. J. Mech. Phys. Solids 56, 2401–2421.

Audoly, B., Boudaoud, A., 2008b. Buckling of a thin film bound to a compliant substrate—Part II: A global scenario for the formation of herringbone pattern. J. Mech. Phys. Solids 56, 2422–2443.

Audoly, B., Boudaoud, A., 2008c. Buckling of a thin film bound to a compliant substrate–Part III: Herringbone solutions at large buckling parameter. J. Mech. Phys. Solids 56, 2444–2458.

Bertoldi, K., Boyce, M.C., Deschanel, S., Prange, S.M., Mullin, T., 2008. Mechanics of deformation-triggered pattern transfromations and superelastic behavior in periodic elastomeric structures. J. Mech. Phys. Solids 56, 2642–2668.

Bowden, N., Brittain, S., Evans, A.G., Hutchinson, J.W., Whitesides, G.M., 1998. Spontaneous formation of ordered structures in thin films of metals supported on an elastomeric polymer. Nature 393, 146–149.

Breid, D., Crosby, A.J., 2009. Surface wrinkling behavior of finite circular plates. Soft Matter 5, 425–431.

Breid, D., Crosby, A.J., 2011. Effect of stress state on wrinkle morphology. Soft Matter 7, 4490–4496.

Budday, S., Kuhl, E., Hutchinson, J.W., 2015. Period-doubling and period-tripling in growing bilayered systems. Philos. Mag. 95, 3208–3224

Cai, S., Breid, D., Crosby, A.J., Suo, Z., Hutchinson, J.W., 2011. Periodic patterns and energy states of buckled films on compliant substrates. J. Mech. Phys. Solids 59, 1094–1114.

Cao, Y., Hutchinson, J.W.,, 2012. From wrinkles to creases in elastomers: the instability and imperfection-sensitivity of wrinkling. Proc. R. Soc. A 468, 94–115.

Chen, X., Hutchinson, J.W., 2004. Herringbone buckling patterns of compressed thin films on compliant substrates. J. Appl. Mech. 71, 597–603.

Combescure, C., Henry, P., Elliott, R.S., 2016. Post-Bifurcation and stability of a finitely strained hexagonal honeycomb subjected to equi-biaxial in-plane loading. Int. J. Solids Struct. 88–89, 296–318.

Combescure, C., Elliott, R.S., Triantafyllidis, N., 2020. Deformation patterns and their stability in finitely strained circular cell honeycombs. J. Mech. Phys. Solids 142, 103976.

Damil, N., Potier-Ferry, M., 1990. A new method to compute perturbed bifurcation: application to the buckling of imperfect elastic structures, Int. J. Eng. Sci. 26, 943–957.

Diab, M., Zhang, T., Zhao, R., Gao, H., Kim, K.S., 2013. Ruga mechanics of creasing: from instantaneous to setback creases. Proc. R. Soc. A 469, 20120753.

DuPont Jr, S.J., Cates, R.S., Stroot, P.G., Toomey, R., 2010. Swelling-induced instabilities in microscale, surface-confined poly(N-isopropylacryamide) hydrogels. Soft Matter 6, 3876–3882.

Flory, P.J., Rehner, J., 1943. Statistical mechanics of cross-linked polymer networks II. Swelling. J. Chem. Phys. 11, 521–526.

Frenkel, J., 1940. A theory of elasticity, viscosity and swelling in polymeric rubber-like substances. Rubber Chem. Technol. 13, 264–274.

Gibson, L.J., Ashby, M.F., 1997. Cellular Solids: Structure and Properties, 2nd Edition. Cambridge University Press, Cambridge.

Golubitsky, M., Stewart, I., Schaeffer, D.G., 1988. Singularities and Groups in Bifurcation Theory, Volume II. Springer, New York.

Guvendiren, M., Yang, S., Burdick, J.A., 2009. Swelling-Induced surface patterns in hydrogels with gradient crosslinking density. Adv. Funct. Mater. 19, 3038– 3045.

Guvendiren, M., Burdick, J.A., Yang, S., 2010a. Kinetic study of swelling-induced surface pattern formation and ordering in hydrogel films with depth-wise crosslinking gradient. Soft Matter 6, 2044–2049.

Guvendiren, M., Burdick, J.A., Yang, S., 2010b. Solvent induced transition from wrinkles to creases in thin film gels with depth-wise crosslinking gradients. Soft Matter 6, 5795–5801.

Healey, T.J., 1988. A group-theoretic approach to computational bifurcation problems with symmetry. Comput. Meth. Appl. Mech.Eng. 67, 257–295.

Healey, T.J., 1989. Why bifurcation: a study of a reticulated dome. In Ang. A.H.-S. editor. Structural Design, Analysis and Testing, 942–948.

Hill, R., 1958. A general theory of uniqueness and stability in elastic–plastic solids. J. Mech. Phys. Solids 6, 236–249.

Hong, W., Liu, Z., Suo, Z., 2009. Inhomogeneous swelling of a gel in equilibrium with a solvent and mechanical load. Int. J. Solids Struct. 46, 3282–3289.

Huang, Z.Y., Hong, W., Suo, Z., 2005. Nonlinear analyses of wrinkles in a film bonded to a compliant substrate. J. Mech. Phys. Solids 53, 2101–2118.

Huck, W., Bowden, N., Onck, P., Pardoen, T., Hutchinson, J.W., Whitesides, G.M., 2000. Ordering of spontaneously formed buckles on planar surfaces. Langmuir 16, 3497–3501.

Ikeda, K., Murota, K., 2002. Imperfect Bifurcation in Structures and Materials: Engineering Use of Group-Theoretic Bifurcation Theory. Springer, New York.

Kang, M.K., Huang, R., 2010a. A variational approach and finite element implementation for swelling of polymeric hydrogels under geometric constraints. J. Appl. Mech. 77, 061004.

Kang, M.K., Huang, R., 2010b. Swelling-induced surface instability of confined hydrogel layers on substrates. J. Mech. Phys. Solids 58, 1582–1598.

Ohno, N., Okumura. D., Noguchi, H., 2002. Microscopic symmetric bifurcation condition of cellular solids based on a homogenization theory of finite deformation. J. Mech. Phys. Solids 50, 1125–1153.

Okumura, D., Ohno, N., Noguchi, H., 2002. Post-buckling analysis of elastic honeycombs subjected to in-plane biaxial compression. Int. J. Solids Strut. 39, 3487–3503.

Okumura, D., Ohno, N., Noguchi, H., 2004. Elastoplastic microscopic bifurcation and post-bifurcation behavior of periodic cellular solids. J. Mech. Phys. Solids 52, 641–666.

Okumura, D., Inagaki, T., Ohno, N., 2015. Effect of prestrains on swelling-induced buckling patterns in gel films with a square lattice of holes. Int. J. Solids Struct. 58, 288–300.

Okumura, D., Kasugai, A., 2016. Eigenvalue buckling analysis of swelling-induced pattern transformation in porous gel films. Trans. Japan Soc. Comp. Eng. Sci. 2016, 20160020 (in Japanese).

Okumura, D., Sugiura, J., Tanaka, H., Shibutani, Y., 2018. Buckling and postbuckling of etching-induced wiggling in a bilayer structure with intrinsic compressive stress. Int. J. Mech. Sci. 141, 78–88.

Papka, S.D., Kyriakides, S., 1999. Biaxial crushing of honeycombs—Part I: experiments. Int. J. Solids Struct. 36, 4367–4396.

Tallinen, T., Chung, J.Y., Biggins, J.S., Mahadevan, L., 2014. Gyrufication from constrained cortical expansion. PNAS 111, 12667–12672.

Tallinen, T., Chung, J.Y., Rousseau, F., Girard, N., Lefèvre, J., Mahadevan, L., 2016. On the growth and form of cortical convolutions. Nature Physics 12, 588–593. .

Tallinen, T., Biggins, J.S., 2015. Mechanics of invagination and folding: hybridized instabilities when one soft tissue grows on another. Phys. Rev. E 92, 022720.

Treloar, L.R.G., 1975. The Physics of Rubber Elasticity, 3rd ed.; Clarendon Press: Oxford.

Xu, F., Potier-Ferry, M., Belouettar, S., Cong, Y., 2014. 3D finite element modeling for instabilities in thin films on soft substrates. Int. J. Solids Struct. 51, 3619–3632.

Xu, F., Koutsawa, Y., Potier-Ferry, M., Belouettar, S., 2015. Instabilities in thin films on hyperelastic substrates by 3D finite elements. Int. J. Solids Struct. 69–70, 71–85.

Yoo, P.J., Suh, K.Y., Park, S.Y., Lee, H.H., 2002. Physical self-assenmbly of microstructures by anisotropic buckling. Adv. Mater. 14, 1383-1387.

Zhao, Y., Zhu, H., Jiang, C., Cao, Y., Feng, X.Q., 2019. Wrinkling pattern evolution on curved surfaces. J. Mech. Phys. Solids 135, 103798.